



Size and Shape of (11351) Leucus from Five Occultations

Marc W. Buie¹ , Brian A. Keeney¹ , Ryder H. Strauss^{2,3}, Ted E. Blank⁴, John G. Moore⁴, Simon B. Porter¹ , Lawrence H. Wasserman⁵ , Robert J. Weryk⁶ , Harold F. Levison¹ , Catherine B. Olkin¹ , Rodrigo Leiva¹ , Jerry E. Bardecker^{2,4}, Michael E Brown⁷ , Lilah B Brown⁸, Michael P. Collins^{4,5}, Hugh M. Davidson⁹, David W. Dunham^{4,10} , Joan B. Dunham⁴, John A. Eaccarino¹¹, Tiffany J. Finley¹, Lindsay Fuller¹², Maria L. Garcia², Tony George^{2,4}, Kai Getrost⁴, Megan, T. Gialluca⁵ , Rima M. Givot^{2,13}, David Gupton^{2,14}, William H. Hanna⁴, Carl William Hergenrother¹⁵, Yimir Hernandez¹¹, Bryan Hill², P. C. Hinton³ , Timothy R. Holt^{1,16} , Robert R Howell¹⁷, Jack Lee Jewell⁴, Roxanne L. Kamin⁴, Joshua A. Kammer¹¹ , Theodore Karet¹⁵ , Gregory J. Kayl^{11,12}, John M. Keller^{2,3} , David A. Kenyon⁴, Scott R. Kester, II¹¹, John N. Kidd, Jr.¹⁵ , Tod R. Lauer¹⁸ , Cecilia W. S. Leung¹⁵, Zoey R. Lorusso², Christopher B. Lundgren², Lizeth O. Magana^{11,12}, Paul D. Maley⁴, Franck Marchis^{19,20} , Robert L. Marcialis¹⁵, Andrew E. McCandless², Delsie Joy McCrystal^{2,13}, Allison Marie McGraw¹⁵, Kelly E. Miller¹¹ , Beatrice E. A. Mueller²¹ , J. W. Noonan¹⁵ , Aart M. Olsen⁴, Alexander R. Patton²², Daniel O'Conner Peluso¹⁶, Michael J. Person²² , James G. Rigby², Alex D Rolfsmeier³, Julien J. Salmon¹ , Joseph Samaniego³, R. P. Sawyer^{11,12} , David M. Schulz²³, Michael F Skrutskie²⁴, Rose J. C. Smith²⁵, John R. Spencer¹, Alessondra Springmann¹⁵ , Dale R. Stanbridge¹⁰, Timothy J Stoffel², Peter Tamblyn¹, Bryan Tobias¹², Anne J. Verbiscer²⁴ , Michael P. von Schalscha², Holly Werts², and Qicheng Zhang⁷

¹ Southwest Research Institute, 1050 Walnut Street, Boulder, CO 80302, USA; buie@boulder.swri.edu

² Research and Education Collaborative Occultation Network, USA

³ University of Colorado—Boulder, 2000 Colorado Avenue, Boulder, CO 80309, USA

⁴ International Occultation Timing Association, USA

⁵ Lowell Observatory, 1400 W. Mars Hill Road, Flagstaff, AZ 86001, USA

⁶ Institute for Astronomy, University of Hawaii, Honolulu, HI, USA

⁷ California Institute of Technology, 1200 E. California Boulevard, Pasadena, CA 91125, USA

⁸ Polytechnic School, Pasadena, CA, USA

⁹ Denver Astronomical Society, P.O. Box 102738, Denver, CO 80250, USA

¹⁰ KinetX Aerospace, 2050 E. ASU Circle, #107, Tempe, AZ 85284, USA

¹¹ Southwest Research Institute, 6220 Culebra Road, San Antonio, TX 78238, USA

¹² University of Texas at San Antonio, 1 UTSA Circle, San Antonio, TX 78249, USA

¹³ Sisters High School, 1700 W. McKinney Butte Road, Sisters, OR 97759, USA

¹⁴ Calipatria High School, Calipatria, CA, USA

¹⁵ Lunar and Planetary Laboratory, University of Arizona, 1629 E. University Boulevard, Tucson, AZ 85721, USA

¹⁶ Centre for Astrophysics, University of Southern Queensland, Toowoomba, QLD 4350, Australia

¹⁷ University of Wyoming, 1000 E. University Avenue, Laramie, WY 82071, USA

¹⁸ NSFs National Optical Infrared Astronomy Research Laboratory, P.O. Box 26732, Tucson, AZ 85726, USA

¹⁹ Unistellar, 19 rue Vacon, F-130001 Marseille, France

²⁰ SETI Institute, Carl Sagan Center, 189 Bernardo Avenue, Mountain View, CA 94043, USA

²¹ Planetary Science Institute, 1700 East Fort Lowell, Suite 106, Tucson, AZ 85719, USA

²² Massachusetts Institute of Technology, Department of Earth, Atmospheric and Planetary Sciences, George R. Wallace Jr. Astrophysical Observatory, Cambridge, MA, USA

²³ Surprise Valley Joint Unified School District, 470 Lincoln Street, Cedarville, CA 96104, USA

²⁴ University of Virginia, Department of Astronomy, P.O. Box 400325, Charlottesville, VA 22904, USA

²⁵ Software Bisque, 862 Brickyard Circle, Golden, CO 80403, USA

Received 2020 June 8; revised 2021 August 2; accepted 2021 August 3; published 2021 September 24

Abstract

We present observations of five stellar occultations for (11351) Leucus and reports from two efforts on (21900) Orus. Both objects are prime mission candidate targets for the Lucy Discovery mission. Combined results for Leucus indicate a very dark surface with $p_V = 0.037 \pm 0.001$, which is derived from the average of the multichord occultations. Our estimate of the triaxial ellipsoidal shape is for axial diameters of $63.8 \times 36.6 \times 29.6$ km assuming that the spin pole is normal to the line of sight. The actual shape of the object is only roughly elliptical in profile at each epoch. Significant topography is seen with horizontal scales up to 30 km and vertical scales up to 5 km. The most significant feature is a large depression on the southern end of the object as seen from a terrestrial viewpoint. For this work we developed a method to correct for differential refraction, accounting for the difference in color between the target object and the reference stars for astrometry derived from ground-based images.

Unified Astronomy Thesaurus concepts: Stellar occultation (2135); Jupiter trojans (874); Astrometry (80)

Supporting material: data behind figures, machine-readable tables

1. Introduction

The NASA Discovery mission Lucy is scheduled to visit five targets in the Jovian Trojan population (Levison et al. 2017). These two captured swarms, located near Jupiter's L4 and L5



Original content from this work may be used under the terms of the [Creative Commons Attribution 4.0 licence](#). Any further distribution of this work must maintain attribution to the author(s) and the title of the work, journal citation and DOI.

Table 1
Occultation Star Data

Star	Epoch (yr)	R.A.(α) (deg)	σ_{α} (mas)	Decl.(δ) (deg)	σ_{δ} (mas)	Parallax (mas)	PM_{α} (mas yr $^{-1}$)	PM_{δ} (mas yr $^{-1}$)	G (mag)
LE20171018	2015.5	280.4243821458	0.030	-15.9057016500	0.029	1.295 \pm 0.038	-2.626 \pm 0.055	-13.712 \pm 0.045	13.72
	2017.794	280.4243800461	0.135	-15.9057104241	0.107
LE20181114	2015.5	310.2150607125	0.048	-7.2228326556	0.034	0.415 \pm 0.060	-3.578 \pm 0.099	-6.362 \pm 0.070	15.75
	2018.868	310.2150572297	0.342	-7.2228386415	0.239
LE20181118	2015.5	310.7044658167	0.026	-7.1951192000	0.018	1.192 \pm 0.038	-19.719 \pm 0.060	-14.871 \pm 0.033	13.97
	2018.879	310.7044468551	0.207	-7.1951332576	0.114
OR20190907	2015.5	318.8532090042	0.067	-6.0698258333	0.049	2.772 \pm 0.050	-5.925 \pm 0.168	-17.377 \pm 0.109	11.68
	2019.684	318.8532017146	0.707	-6.0698460404	0.459
LE20191002	2015.5	340.2921187042	0.023	6.7607762861	0.021	2.778 \pm 0.027	5.430 \pm 0.051	-21.372 \pm 0.037	13.52
	2019.751	340.2921249766	0.218	6.7607510649	0.159
OR20191104	2015.5	317.7982223208	0.028	-7.5331630111	0.023	0.536 \pm 0.031	-2.091 \pm 0.055	-6.836 \pm 0.044	13.12
	2019.842	317.7982196324	0.242	-7.5331713043	0.193
LE20191229	2015.5	343.2505298750	0.039	4.3432345583	0.031	1.665 \pm 0.048	0.183 \pm 0.075	-2.278 \pm 0.057	10.88
	2019.992	343.2505297201	0.341	4.3432315226	0.259

Note. Positions are all referenced to EME2000. The stars are named for the events, with the first two characters coming from the first two letters of the occulting body, while the numbers are a packed form of the UT date of the event. The at-epoch positions provided are computed using only these attributes of the sources from the Gaia DR2 catalog.

Lagrange points, are vital to our understanding of the early solar system (Nesvorný 2018; Holt et al. 2020). The population also contains a diversity of taxonomic types (DeMeo et al. 2009; Grav et al. 2012), with possible links to the outer solar system populations (Emery et al. 2015; Wong & Brown 2016). The work discussed here is in regard to (11351) Leucus, a D-type object (Fornasier et al. 2007), and to a lesser extent (21900) Orus, both of which are among the selected targets for Lucy.

One of Lucy’s goals is to measure the bulk density of all targets. The masses will be directly measured from the gravitational deflection of the spacecraft during each flyby. The volume of the body must also be measured, and the imaging science experiments will obtain limb and topography data. Of the mission targets, Leucus has the longest rotational period at roughly 446 hr (Buie et al. 2018). Due to this slow rotation period and the speed of the flyby, the imaging data will not provide complete coverage of the entire body. To more fully constrain the shape and dimensions of each target, the Lucy project is using Earth-based stellar occultation observations.

This work builds on the successful characterization of (486958) Arrokoth, the New Horizons Kuiper Belt Extended mission target (Buie et al. 2020). Those observations for Arrokoth paved the way for dense and highly coordinated stellar occultation observing campaigns. Tightly targeted observations are not possible without the accurate stellar positions of the target stars provided by the Gaia mission. We used positions from the second data release (DR2), described in Brown et al. (2018). Unlike Arrokoth, we also had direct measurements of Leucus provided in DR2 to further constrain the orbit and ground-based telescopic observations that could also be used to support the predictions.

Leucus inhabits the L4 (leading, Greek camp) Jupiter Trojan swarm. Its absolute magnitude is $H_r = 11.046$ (Buie et al. 2018). The Infrared Astronomical Satellite provided a size estimate of $D = 42$ km (Tedesco et al. 2002). Wide-field

Infrared Survey Explorer data from Grav et al. (2012) provided a diameter of 34 km. The albedo derived by Buie et al. (2018) was 0.047, with a light-curve amplitude of 0.6 mag. We chose to base our ground-track predictions on $D = 34$ km and absorb the uncertainty in the size and variation in size with rotation as a systematic error component of 10 km that was included in the prediction uncertainty.

Our organized campaigns began in 2018 with the identification of two Leucus events just 4 days apart in roughly the same region of the United States. These were preceded by independent efforts for a Leucus event in 2017. At the time of our first Leucus campaign in 2018, we knew of a single chord from an International Occultation Timing Association (IOTA) observer. This event is also presented in this work, as it was crucial to support our prediction work and continued orbit estimations. The original plan was to concentrate on other Lucy targets after the 2018 events, but there were two additional Leucus opportunities in 2019 that we were able to pursue with higher-risk deployments. We present the combined results of these five events along with the results of two additional occultation efforts involving Orus upon which important developments affected the predictions and results for the Leucus events. The larger task of deriving a full three-dimensional shape with a full rotational state is left for a follow-on effort and will not be addressed here.

The star positions for all events are summarized in Table 1. Organization of this paper is largely sequential through the series of seven occultation campaigns discussed here. The planning and deployment for each event were guided by the prior events, as well as ongoing astrometry and orbit improvements. The important elements of that progression are captured as each event is discussed. However, the results of each event are presented relative to the final orbit estimate that was produced at the end of the project. This style of occultation deployment is based on a tightly coordinated approach, and all sites are very close to each other, not just relative to the occultation shadow but close on the scale of the object as well.

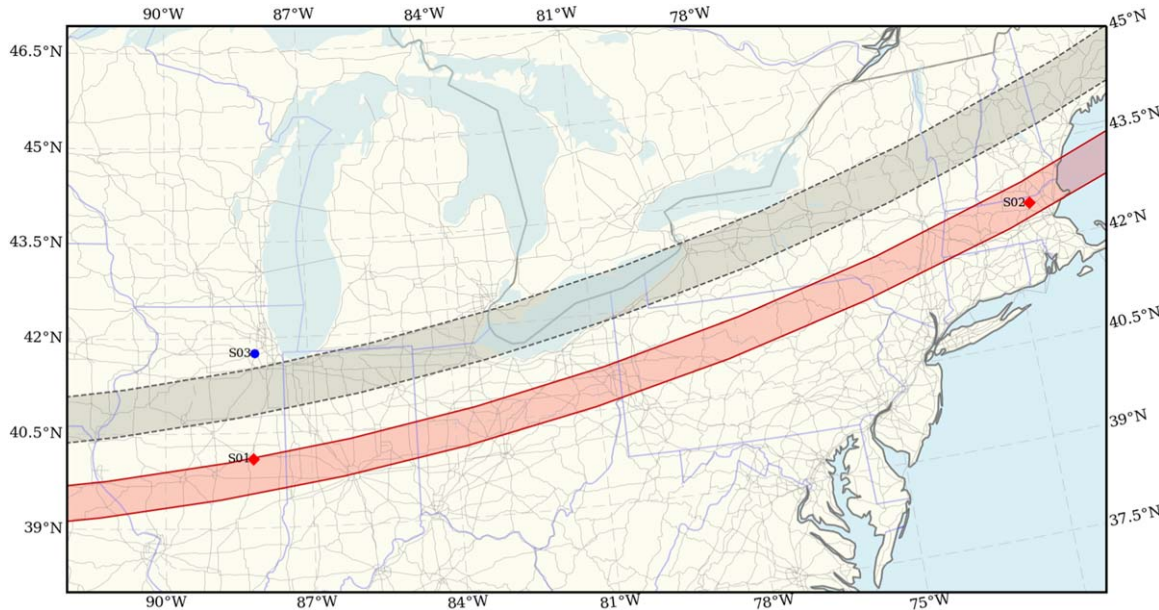


Figure 1. Map of the LE20171018 occultation. The gray region delimited by dashed lines represents the predicted track with a notional diameter of 45 km. The red shaded region delimited by solid lines shows the actual occultation zone. The observing locations are shown labeled by their site codes. Blue circles indicate good data with no occultation. Red diamonds indicate good data with a positive occultation detection. Faint gray lines show major highways.

Table 2
Observing Stations and Teams for 2017 October 18

ID	UT Start	UT End	Lat (deg)	Lon (deg)	Alt (m)	Observers	Offset (km)
S03	00:00:00	00:02:20	41.758889	-088.116722	230	R. Dunford	36
S01	23:59:28	00:03:07	40.086778	-088.196190	224	A. Olsen	-66
S02	00:01:43	00:02:36	42.610278	-071.483889	81	M. Person	-87

Note. All times are on 2017 October 18. All site locations are referenced to the WGS84 datum. Offset is the distance perpendicular to the centerline of the last prevent prediction.

We will provide results from six successful occultations and combine these results to provide details we can deduce about Leucus and Orus. Finally, we provide appendices with a more in-depth discussion about our astrometry and orbit fitting process.

2. Event 1—LE20171018

Prior to the Lucy-coordinated campaigns, an event was noted by IOTA, and one successful chord was reported by a successful IOTA observer. Later, another positive detection from the MIT occultation group and a negative detection from another IOTA observer were reported. This event was independently found by Felipe Braga Ribas and colleagues in Brazil collaborating with the Lucky Star Project;²⁶ they informed IOTA, which incorporated the event into their prediction system and encouraged observations of it. Efforts to observe the event were definitely influenced by Leucus being a Lucy target and self-driven by these observers rather than through coordination with the Lucy Mission team. The prediction was not accurate enough to ensure that any given station would be successful, and this type of event prediction is rarely acted upon without some special motivation. The predicted and final ground tracks of the shadow are shown in Figure 1.

²⁶ <https://lesia.obspm.fr/lucky-star>

Table 3
Equipment and Settings for 2017 October 18 Data

ID	Ap (cm)	Camera	ExpTime	Timing	Mount
S03	35.6	Wattec 910BD	PAL 4x	VTI	TZ
S01	50.0	Wattec 910BD	PAL 2x	VTI	TZ
S02	61.0	ZWO ASI174MM	~0.75s	GPSi	EQ

Note. EQ—equatorial mount; TZ—alt/az mounts; VTI—video-time inserter (GPS base). GPSi—GPS data used to control system clock, image timing from the controlled clock. PAL—video signal type with field integration factor given (approximate exposure time is the given factor multiplied by 40 ms).

The event prediction generated by IOTA indicated an event on 2017 October 18 UT; see Table 1 for the star information. Their cross-track uncertainty at that time was 31 km, and the success probability for any given site was much lower than usual for events typically observed by IOTA participants. The star was faint enough that only a small fraction of IOTA members had the equipment necessary to observe such an event. We do not report on an actual deployment plan here. The important fact to note is that the successful observations came from a few observers setting up in their natural locations rather than embarking on a mobile deployment.

The observing stations for this event are listed in Table 2, and the equipment used is listed in Table 3. The equipment for S01 and S03 has been extensively used within the IOTA

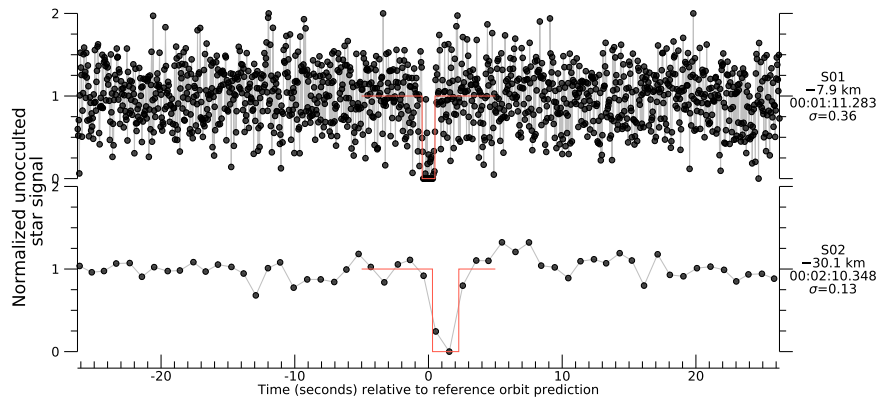


Figure 2. Light curves for LE20171018. The plots are clipped at 0 and 2.0 for clarity. The labels on the right identify the team, the cross-track offset relative to the final prediction, the reference mid-time, and the standard deviation of the per-point scatter. The positive detection occultation model (red) is shown as well. The data used for the figure (without clipping) are provided in electronic form.

(The data used to create this figure are available.)

Table 4
Occultation Timings 2017 October 18

Team ID	UT Disappearance	UT Reappearance	Length (km)	Offset (km)
S01	00:01:10.810 \pm 0.012	00:01:11.768 \pm 0.012	18.9 \pm 0.3	-60
S02	00:02:10.643 \pm 0.122	00:02:12.624 \pm 0.120	39.1 \pm 3.4	-87

Note. All times are on 2017 October 18. Offset is the distance perpendicular to the centerline of the last pre-event prediction.

community and beyond, and the photometric and timing characteristics are well understood (Dangl 2013), providing time-tagged data good to at least 1 ms after the camera and video time delays are applied. The data from site S02 were collected with the newly commissioned Elliot 24-inch telescope at MIT’s Wallace Astrophysical Observatory. In fact, these were the first science data acquired by that telescope. The Elliot-24 is a PlaneWave CDK telescope, and the camera was a ZWO ASI174MM Monochrome Cooled imager controlled by SharpCap software. The instrument computer was GPS time synced, and the GPS software reported a <2 ms timing error throughout the data collection. Image frames were triggered by SharpCap at approximately a 0.75 s cadence with minimal dead time. The data were acquired unfiltered. Calibrated intensities were extracted using aperture photometry with the full signal level being normalized to 1.0 and the Leucus-only brightness (“zero level”—calibrated from separated photometry taken after the event) being set to 0.0, resulting in the plotted integrated stellar signal.

The light curves with positive detections can be seen in Figure 2. The red curve overlaid on the data is the occultation model fitted to the data. This model consists of a simple square function that assumes that the star signal is instantly turned off (or on) by the limb of the occulting body. Furthermore, the flux of the star is set to 1 when visible and 0 when occulted, and the residual flux from the target is either subtracted (as is the case for this event) or set to 0 (as is the case for the other events). This model explicitly assumes that the stellar diameter is small enough to be ignored. Also, all diffraction effects are ignored owing to our relatively slow sampling rate. The derived timing is used to define the edges of the model occultation. This fitting approach is used for all of the events analyzed in this paper. The timing uncertainty is derived from a combination of the photometric uncertainty in the light-curve data and the

assumption that only one image or the boundary between two images will contain the disappearance or reappearance. Most of the time this transitional frame is obvious, and where not, the images are carefully examined to select the most likely transitional frame. The timings extracted for these chords are listed in Table 4. As shown by the data, the actual shadow was south of the prediction by just over 2σ . Based on the original prediction and the actual projected object size, the probability of seeing an event for site S03 was 21%, while the probability of S01 was 6% and that of S02 was 1.5%. The joint probability of the observed outcome was just 1.4%, and it is no exaggeration to describe this observation as a lucky success.

Combining the geometric information for the occultation results in the geometric constraints plotted in Figure 3. The large orange circles are the disappearance and reappearance constraints plotted on the sky plane at the object. The small orange circles show the 1σ uncertainty estimates on these timing measurements. The predicted center based on our final orbit fit defines the origin of this plot. Time moves from right to left for this event. Our normal procedure is to perform a weighted least-squares fit of an ellipse to the timing values once converted to sky-plane position at the object. The solid cyan line is from the fit to the edge detections (large orange circles) weighted by the timing uncertainties. Each fit solves for five unknowns, the position of the center, the semimajor and semiminor axes, and the position angle of the major axis on the plane of the sky. The dashed cyan lines show the result of two other bounding fits. One fit takes the disappearance time adjusted by -1σ (early) and the reappearance time adjusted by $+1\sigma$ (later) to constrain the ellipse fit, making for a larger ellipse. The other fit changes the sign on the adjustment for a smaller ellipse. These dashed lines can give some crude indication of the uncertainty in the ellipse fit. See Appendix A

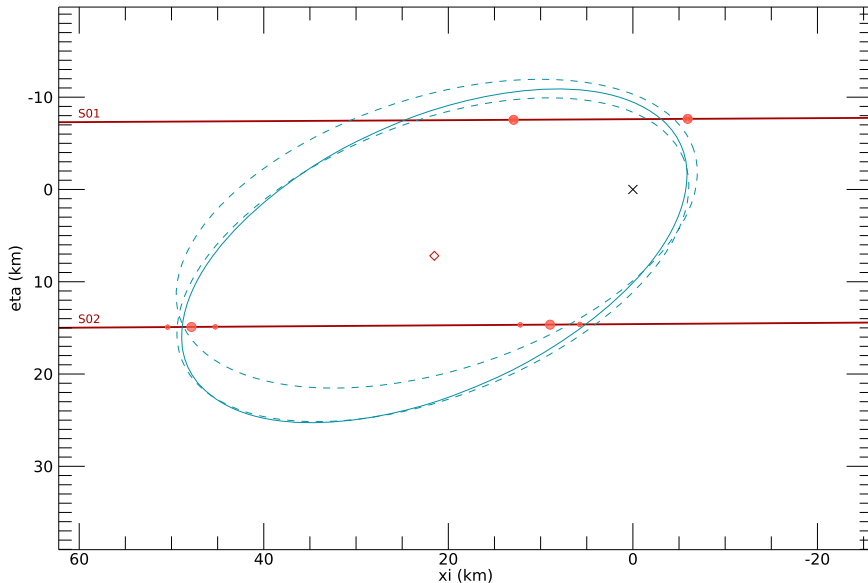


Figure 3. Limb profile for LE20171018. Shadow plane projection of occultation timing. These are tangent plane positions oriented as if looking down on the projected shadow as it would appear on the surface of Earth (see Appendix A for details). Orange circles are the measurements from Table 4; their individual (ξ , η) values are available in a machine-readable format (Table 17). The 1σ uncertainties, when visible, appear as half-size circles. The labeled lines show the track of the star across the object as seen at each site. The cross indicates the predicted center based on the final orbit estimate. The diamond symbol indicates the center of the fitted ellipse.

for a more complete description of this plot and its coordinate system.

In the case of this event, an unconstrained fit to these four occultation points produced an ellipticity and projected area that were inconsistent with both the light curve of the object and the other four occultations. Figures 2 and 3 both show a significant time shift between the two chords where the centers are shifted by ~ 25 km or about 1.3 s. We know that the underlying timing accuracy of the images is good to 1 ms. The uncertainty due to the measured time of disappearance and reappearance is larger but still more than an order of magnitude smaller than the observed shift, thus giving us confidence that the time shift is real. We then searched for an elliptical profile that could both explain the data and yet remain reasonably consistent with other data sets. Our final estimate for a fitted ellipse is shown in Figure 3 and is the result of a restricted fit where the axes are forced to be 29.3×14.8 km. These constrained values are generated from the final shape results of this paper, where the semimajor axis is set to a value that gives a projected area consistent with the light-curve constraints. Additionally, the position angle is forced to be within 8° of the average position angle measured in the later events. The allowed range is set by the range in fitted position angle for all events. The position of the ellipse is the only unconstrained free parameter in the fit. The resulting ellipse is a reasonably good fit to the data, though the residuals are much larger than the uncertainties for the S01 constraints. As will be seen in the subsequent data, there is considerable topography on Leucus, and these post-fit residuals are not concerning.

The center of the S01 chord was taken to be the center of the object for the purposes of predicting the next two campaigns. At that time we did not yet have the S02 chord, whose inclusion would clearly have improved the prediction. Our choice clearly introduced a small offset from the true body center, leading to a slight error in the predictions. The introduced error was much smaller than the overall correction provided by using S01 as we did. This case provides an important proof of concept for using even a single-chord event

to update an ephemeris and provide a subsequent prediction good enough for a successful high-density targeted occultation campaign described in the next two sections. Without this first successful event, the next two events would have required a much larger footprint of the deployed station, leading to a significantly smaller number of chords across the body.

3. Event 2—LE20181114

This event was the first coordinated campaign conducted by the Lucy project. The deployment location options and proximity in time to the next event were strong factors in the decision to pursue this event. The target star was anticipated to be at the limit of our occultation systems and likely would not have been attempted without the other considerations.

3.1. Prediction

The prediction for this event was driven by our normal automatic orbit fit based on available Minor Planet Center (MPC) data. This orbit provides the same starting point as for the Research and Education Collaborative Occultation Network (RECON; Buie et al. 2018) and was used to generate a prediction for both LE20171018 and this event. An R.A. offset of -0.0026 s and decl. offset of $-0.^{\prime\prime}021$ when applied to the ephemeris gave a “prediction” for LE20171018 that was consistent with the S01 chord seen, assuming that it was a central chord. This same offset was then applied to the ephemeris for the LE20181114 prediction. In our opinion such a procedure is a poor substitute for proper orbit fitting work, especially with a year between events, but that correction was better than doing nothing. The nominal 1σ cross-track uncertainty without the prior occultation was 80 km. We adopted an estimated uncertainty of 5 km after adding the occultation constraint from LE20171018. We learned afterward that this uncertainty was too small, but the spread of the deployed stations made up for this underestimate.

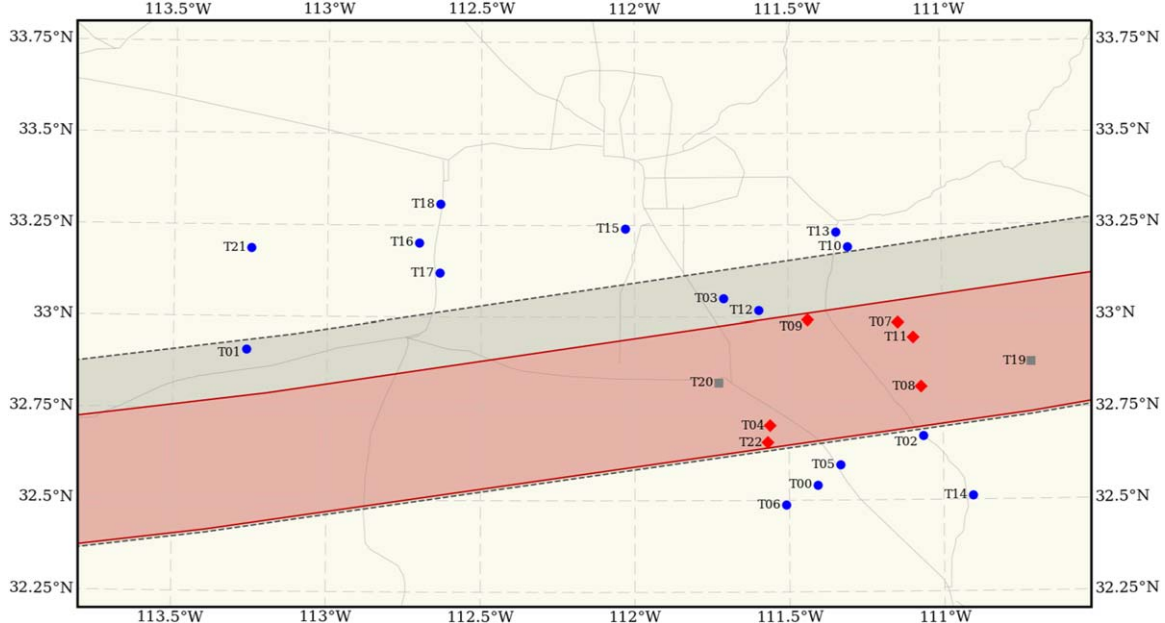


Figure 4. Map of the LE20181114 occultation. The gray region delimited by dashed lines represents the predicted track with a notional diameter of 45 km. The red shaded region delimited by solid lines shows the actual occultation zone. The observing locations are shown labeled by their site codes. Blue circles indicate good data with no occultation. Red diamonds indicate good data with a positive occultation detection. Gray squares indicate sites unable to collect useful data. Faint gray lines show major highways.

Table 5
Mobile Observing Stations and Teams for 2018 November 14

ID	UT Start	UT End	Lat (deg)	Lon (deg)	Alt (m)	Observers	Offset (km)	Comment
T18	03:02:56	03:12:56	33.308783	-112.634608	251	R. Marcialis, J. Spencer	47.5	
T21	03:03:00	03:13:00	33.186490	-113.248337	295	C. Hergenrother, H. Levison	43.8	
T16	03:02:55	03:12:56	33.203107	-112.702140	227	L. Wasserman, T. Karetta	38.7	
T15	03:03:00	03:13:00	33.240654	-112.030774	341	R. Kamin, H. Harris	34.0	
T17	03:03:00	03:13:01	33.119559	-112.635655	260	A. Zangari, C. Leung, R. Hatano	30.3	
T13	03:03:01	03:13:02	33.230786	-111.344593	564	T. Blank, M. Gialluca	24.9	
T10	03:03:01	03:13:03	33.189838	-111.307599	560	J. Salmon, P. Facuna	20.8	
T01	03:03:01	03:13:03	32.909790	-113.263706	179	T. Finley, B. Mueller	18.8	
T03	03:02:59	03:13:00	33.049866	-111.711427	414	W. Hanna, J. Noonan	12.8	
T12	03:03:03	03:13:04	33.017989	-111.596534	418	P. Tamblyn, R. Cunningham	8.5	
T09	03:03:00	03:13:01	32.991927	-111.436632	455	S. Porter, W. Boynton	4.3	
T07	03:03:00	03:13:01	32.982513	-111.144214	790	C. Olkin, A. Springmann	0.0	
T11	03:03:00	03:12:59	32.942445	-111.096097	881	R. Smith, J. Kidd	-4.2	
T20	03:03:01	03:13:01	32.821616	-111.726493	454	J. Scotti, A. McGraw	-7.8	
T19	32.875801	-110.711515	645	D. Dunham, J. Dunham	-15.1	On the wrong field Did not align on field in time
T08	03:03:30	03:13:30	32.809514	-111.070977	928	A. Olsen, K. Volk	-16.6	
T04	03:03:00	03:13:02	32.704691	-111.560651	482	B. Keeney, M. Smith	-20.4	
T22	03:03:03	03:13:03	32.657810	-111.569478	700	J. Bardecker, S. Insana	-24.5	
T02	03:03:10	03:13:12	32.675152	-111.064292	904	K. Getrost, J. Compton	-29.0	
T05	03:03:00	03:12:59	32.597111	-111.334244	564	J. Moore, T. Holt	-33.0	
T00	03:03:06	03:13:05	32.542216	-111.408128	553	M. Buie, M. Devogele	-37.1	
T06	03:03:00	03:13:00	32.487259	-111.510123	634	S. Moss, H. Davidson	-40.9	
T14	03:02:58	03:12:57	32.512134	-110.905255	969	R. Howell, T. Lauer	-45.8	

Note. All times are on 2018 November 14. All site locations are referenced to the WGS84 datum. Offset is the distance perpendicular to the centerline of the last pre-event prediction.

3.2. Deployment

We used our full inventory of 23 SkyWatcher 40 cm Dobsonian telescopes coupled with QHY174M-GPS cameras. All systems were identical. They use GPS time-tagging for all images, and the telescopes have computer-controlled alt/az mounts. A more complete description of this equipment can be found in Buie et al. (2020). The deployment locations are

shown in Figure 4, along with the prediction (gray dashes) and the actual location and size of the shadow path (red shaded region).

The deployed stations are listed in Table 5. The target cross-track spacing between stations was 4 km, and the goal given to each team was to be within 200 m of their assigned track. This plan covered 88 km in the cross-track direction centered on the

predicted centerline. With a notional size of 45 km and uncertainty of 5 km, this deployment plan was equivalent to coverage of $\pm 4.3\sigma$.

3.3. Observations

The weather was not uniform across our deployment zone. Some sites had to contend with cirrus, mostly in the northern half. There was also generally a lot of wind affecting all stations, some more than others. These SkyWatcher telescopes are known to be susceptible to wind. Noticeable wind shake starts to set in at about 10 mph (4.5 m s^{-1}), and by 20 mph (9 m s^{-1}) the image motion prevents collecting any useful data. Due to the wind, the exposure times were set to a faster rate than would otherwise be used. With no wind or clouds and reasonable seeing, the data quality would have been reasonable, but the margin was slim. All stations used an exposure time of 350 ms.

3.4. Photometric Analysis

These data were processed in the same manner as for the Arrokoth occultation campaigns described in Buie et al. (2020). Point-spread function (PSF) fitting was used to get positions and fluxes of all sources, and then an astrometric solution (also known as a World Coordinate System, or WCS) was derived for each frame to map from image pixels to celestial coordinates. At this point, we computed a PSF fit to the target star where the only free parameter was the star flux, and the location is fixed by the WCS solution and the Gaia DR2 star position (Brown et al. 2018). Data within 150 images (± 52.5 s) of the predicted event mid-time for each site were processed. The normalized light curves for each site are shown in Figures 5 and 6.

The signal-to-noise ratio (S/N) of these light curves is low, and there are many dropouts due to wind shake. The data from T09 are clearly the best where an occultation is seen. From there it is possible to then identify the critical data in the other nearby tracks by looking for correlated dropouts. The timing uncertainties on the events are significantly influenced by the data quality. The analyses of these data were sufficiently difficult that only a very small fraction of the data were processed prior to the next event. We only had time to determine that Leucus was basically in the right location, thus validating the prediction, but not good enough to allow any refinement.

3.5. Result

Of the 23 deployed stations, 21 were able to collect useful data. Out of the useful data, 6 out of 21 stations recorded a positive detection. The timing for the occultation is summarized in Table 6. It is clear from these data that the actual shadow was offset about 10 km south of the prediction as seen in the red track plotted in Figure 4, and the projected size of the shadow was less than expected.

The geometry of this event is shown in Figure 7. This plot is of the tangent plane centered on the target star, converted to the spatial scale at Leucus at the time of the event. Thus, if the star position and Leucus orbit had no error, the center of the object should fall at zero on this plot. The position of the origin is shown with a cross, while the center of the fitted ellipse is

marked with a diamond symbol. Our final astrometry from this event is listed in Table 19 in Section 10.

The orientation of the object clearly has the major axis of the elliptical shape mostly parallel to the down-track direction. The cross-track projection of the shape was between 28.8 and 37.5 km. The first number comes from the spread between the outermost sites with positive detections, while the second number is the spread between the first sites with a nondetection. If the elliptical fit to the data is applicable, then the true cross-track size appears to be about halfway between these extremes at 33.2 km. This result has the largest uncertainty of all these events. Even so, the data do suggest nonnegligible topography on the limb at this aspect, though the shape is reasonably well represented by an ellipse.

4. Event 3—LE20181118

This event occurred just 4 days after the prior observation but involved a significantly brighter star. We used the same equipment for this event as for LE20181114, with some observers in common between the two campaigns.

4.1. Prediction

The prediction for this event was done in the same way as for LE20181114, with the same offset based on LE20171018 given in Section 3.1. The adopted uncertainty was again set to 5 km. The general deployment area was originally expected to be in between San Antonio and Austin, TX, but in the final hours before deployment the prediction shifted to the south.

4.2. Deployment

Our style of deployment provides very tight control over the makeup of the teams and the deployment locations, with a typical goal of choosing observing locations good to 10% of the site spacing. A 5 km spacing would thus lead to a requirement of being within ± 250 m of each assigned track. In our experience, this style of deployment is most effective when working from a central location as a means to facilitate this level of coordination. For example, this event required a last-minute relocation of the entire team owing to weather factors. The consequences of this shift go beyond a simple notice to relocate, and we were able to easily work as a team to discuss options for choosing new observing locations. Figure 8 shows the final deployment locations with both the prediction and the actual track.

4.3. Observations

The deployed stations are listed in Table 7. As for the previous event, the target cross-track spacing between stations was 4 km. The weather was clear and calm for the western locations. Shortly after the event was over, the weather rapidly deteriorated with widespread clouds and rain, and we were very fortunate to obtain these results. The data quality for all teams that collected data was excellent. All stations used an exposure time of 250 ms.

4.4. Photometric Analysis

The full data set is shown in Figures 9 and 10. These data were extracted with the same PSF-fitting process described in Section 3.4. The S/N of these light curves is very good, with

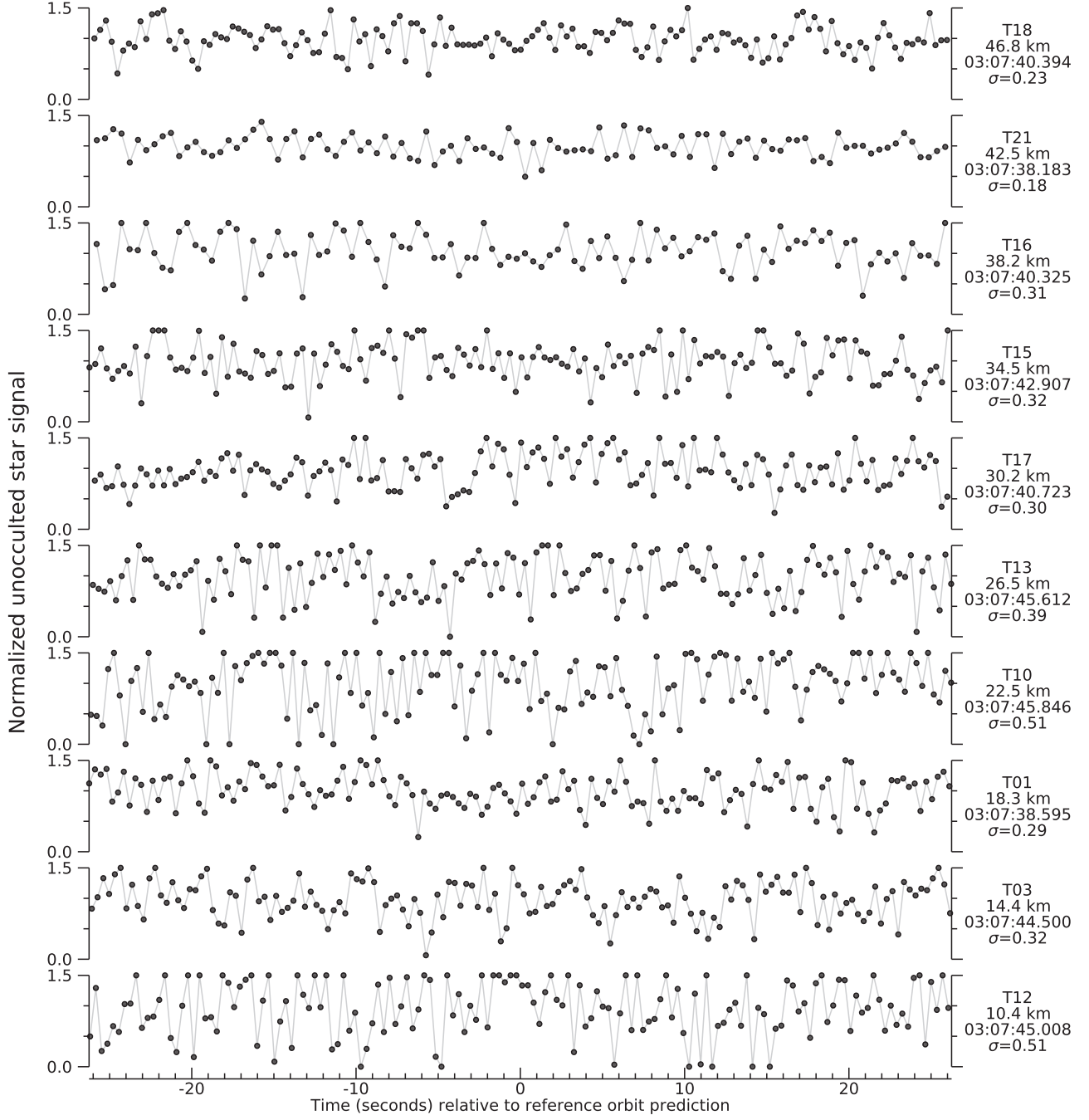


Figure 5. Light curves for LE20181114, part 1. The plots are clipped at 0 and 1.5 for clarity. The labels on the right identify the team, the cross-track offset relative to the final prediction, the reference mid-time, and the standard deviation of the per-point scatter. For those events with a positive detection, the occultation model (in red) is shown as well. The data used for the figure (without clipping) are provided in electronic form.

(The data used to create this figure are available.)

only some minor transparency variations afflicting the observations well away from the occultation (such as those seen at station T01). The timing uncertainty for the star disappearance and reappearance is low, generally about 20–40 ms. Of the 23 deployed stations, 9 recorded a positive detection, and 12 recorded a nondetection. The cross-track size of the shadow was 32.0 km at a minimum. Both other outermost chords were very short, meaning that the actual width could not have been very much bigger. Once again, this

size was smaller than expected, and the actual shadow path was shifted slightly to the south of the prediction, but still covered by the deployed teams.

Some of the data sets, such as for T06, exhibit gaps in the reported light curves. The missing data points correspond to images where the image quality was so bad that the automatic PSF-fitting software failed and did not return a valid result. For this event, this was always due to excessive wind shake of the telescope during the exposure. It is possible to extract a

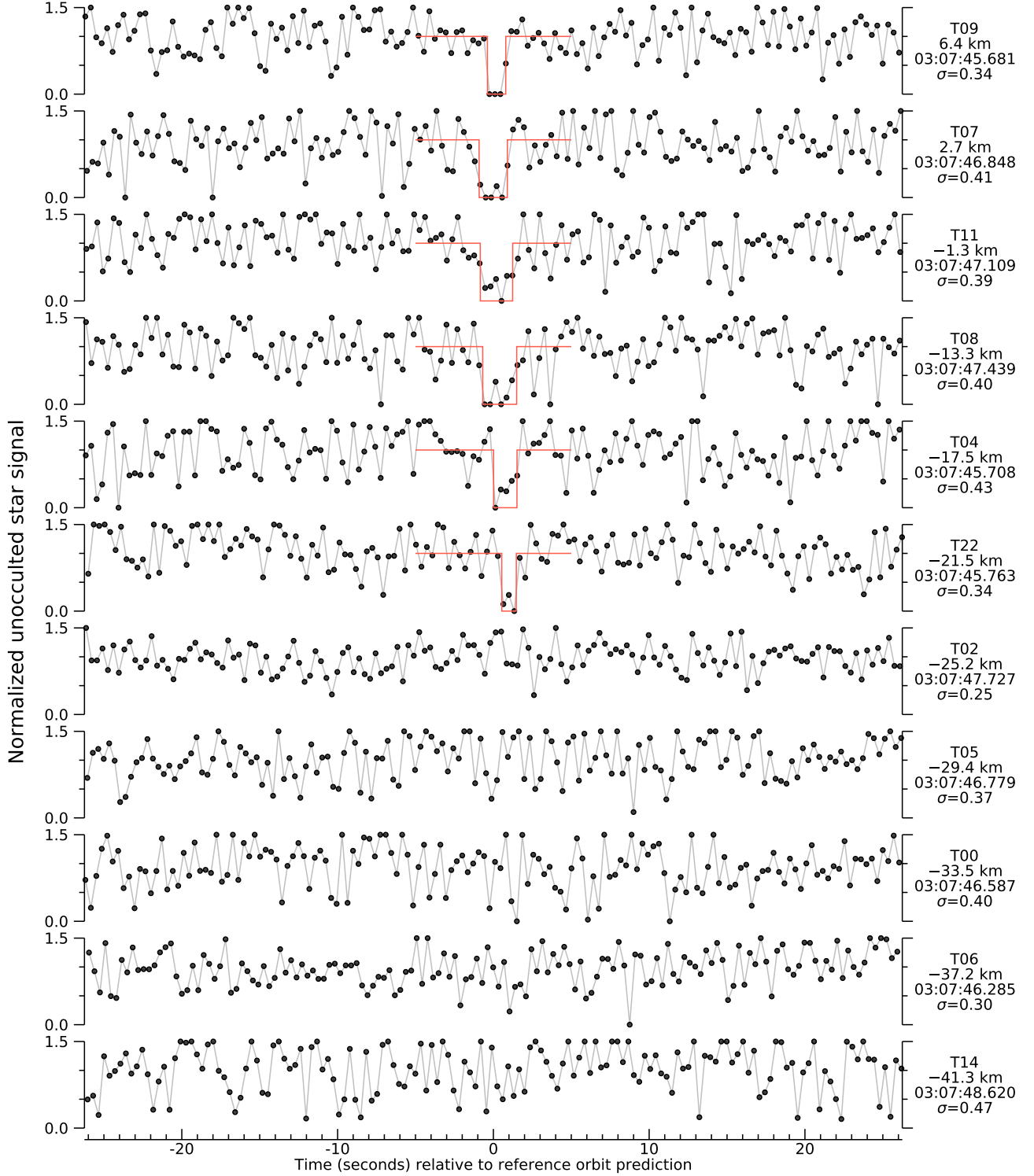


Figure 6. Light curves for LE20181114, part 2. The plots are clipped at 0 and 1.5 for clarity. The labels on the right identify the team, the cross-track offset relative to the final prediction, the reference mid-time, and the standard deviation of the per-point scatter. For those events with a positive detection, the occultation model (in red) is shown as well. The data used for the figure (without clipping) are provided in electronic form.

(The data used to create this figure are available.)

star signal from these frames, but it requires a considerable amount of manual effort with current tools. The same is true for other large excursions well separated from the correlated occultation dips (such as seen at station T16, which was also affected by wind). The level of effort to repair

these data points was reserved for critical values where the effort is important for the shape results. In the case of T06, T16, and T18, the adjacent data sets showed nothing of interest, and we chose to avoid the extra work in these and similar cases.

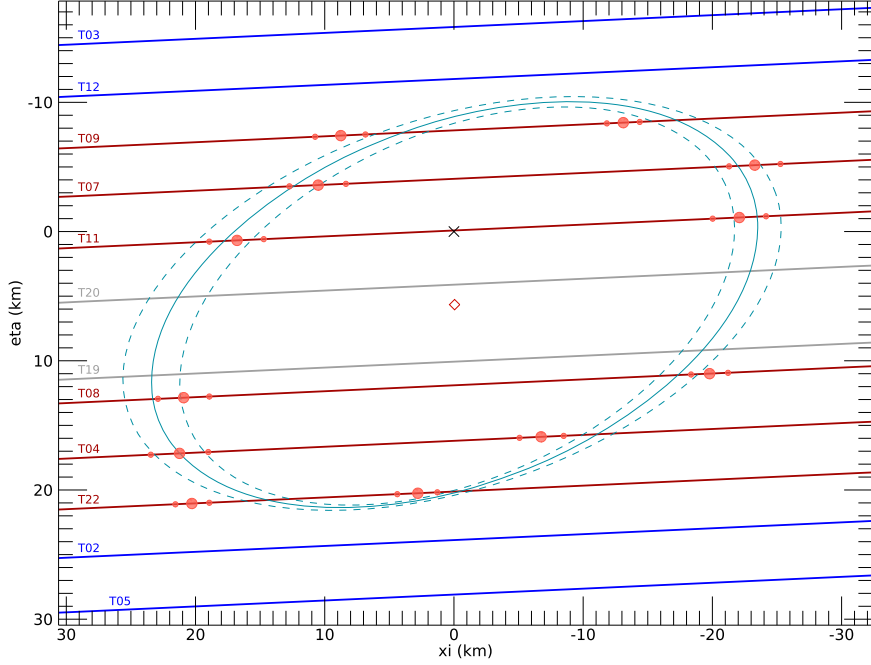


Figure 7. Limb profile for LE20181114. Shadow plane projection of occultation timing. These are tangent plane positions oriented as if looking down on the projected shadow as it would appear on the surface of Earth (see Appendix A for details). Orange circles are the measurements from Table 6; their individual (ξ , η) values are available in a machine-readable format (Table 17). The 1σ uncertainties, when visible, appear as half-size circles. The labeled lines show the track of the star across the object as seen at each site. Orange lines correspond to sites with positive detections, blue lines correspond to sites with negative constraints, and gray lines indicate sites unable to collect useful data. The cross indicates the predicted center based on the final orbit estimate. The diamond symbol indicates the center of the fitted ellipse.

Table 6
Occultation Timings 2018 November 14

Team ID	UT Disappearance	UT Reappearance	Length (km)	Offset (km)
T09	03:07:45.303 ± 0.069	03:07:46.474 ± 0.103	21.9 ± 2.3	4.3
T07	03:07:45.935 ± 0.107	03:07:47.744 ± 0.117	33.8 ± 3.0	0.0
T11	03:07:46.269 ± 0.110	03:07:48.351 ± 0.113	38.9 ± 2.9	-4.2
T08	03:07:46.758 ± 0.076	03:07:48.933 ± 0.106	40.7 ± 2.5	-16.6
T04	03:07:45.723 ± 0.090	03:07:47.226 ± 0.122	28.1 ± 2.8	-20.4
T22	03:07:46.302 ± 0.084	03:07:47.232 ± 0.072	17.4 ± 2.0	-24.5

Note. All times are on 2018 November 14. Offset is the distance perpendicular to the centerline of the last pre-event prediction.

4.5. Result

The timing of this event is summarized in Table 8, and its geometry is shown in Figure 11. As before, the object center is taken to be the center of a fitted ellipse. Clearly, in this case an ellipse is not very good at representing the shape of the object. There are significant departures from an elliptical profile that are much larger than any timing errors. We assume that these departures are due to topography on the body. This profile is consistent with a body that is highly battered from a history of collisions.

5. Event 4—OR20190907

This event was our first attempt at an occultation involving Orus. The Lucy project was not planning to pursue this event, but F. Marchis initiated contact and offered to mount a limited effort to observe using his Unistellar systems on the coast of Oman (Marchis et al. 2020). Figure 12 shows a map of the prediction (gray) and a notional track that is consistent with the

data. The cross-track offset between the observing stations is 21.3 km.

This was our first dedicated prediction with a customized orbit estimate to support the occultation for any Lucy target. At this point in our understanding, we were using data sets known to be based on Gaia DR2 with good uncertainties at full weight while deweighting any historical data for which the support catalog was unknown or did not provide uncertainties. Full details of the prediction work are listed in Appendix B. The formal cross-track uncertainty for this prediction was 2.6 km. The notional diameter adopted for the prediction was 51 km. The amount of deweighting for the historical data was guided by the requirement for the residuals to be reasonable given the weights assigned to the different data sets. If these data were used at too high of a weight, the residuals for the other data sets would be too large given their uncertainties. The decision on weighting is one that unfortunately depends on our judgment for this astrometry. The prediction for the occultation will also change by nontrivial amounts compared to the size of the

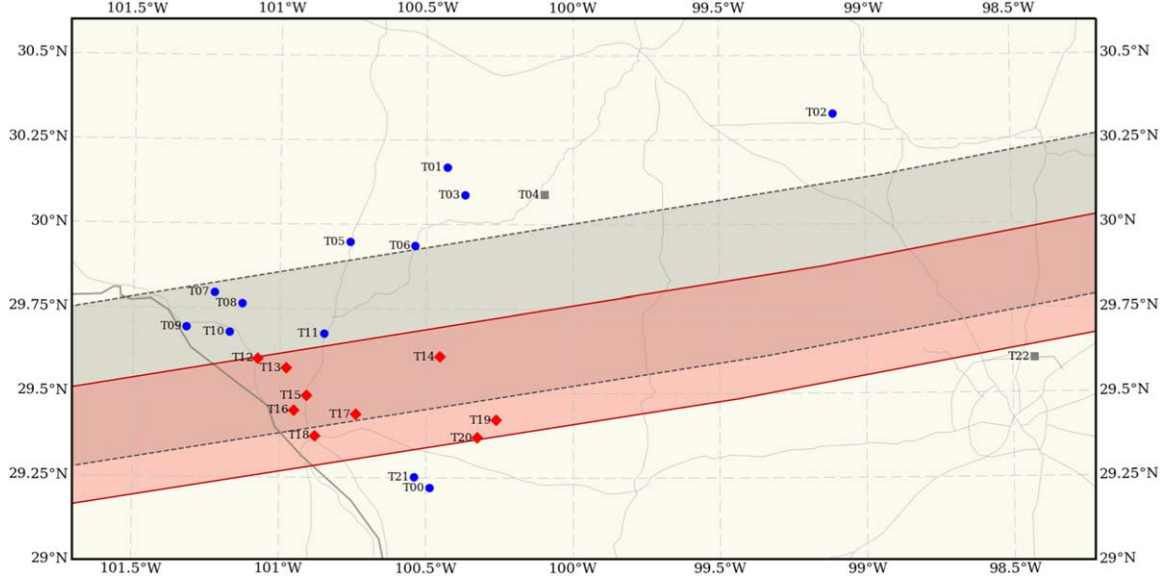


Figure 8. Map of the LE20181118 occultation. The gray region delimited by dashed lines represents the predicted track with a notional diameter of 45 km. The red shaded region delimited by solid lines shows the actual occultation zone. The observing locations are shown labeled by their site codes. Blue circles indicate good data with no occultation. Red diamonds indicate good data with a positive occultation detection. Gray squares indicate sites unable to collect useful data. The border between Texas and Mexico appears in the lower left corner of the map. Faint gray lines show major highways.

Table 7
Mobile Observing Stations and Teams for 2018 November 18

ID	UT Start	UT End	Lat (deg)	Lon (deg)	Alt (m)	Observers	Offset (km)	Comment
T01	02:37:30	02:47:31	30.168745	-100.430637	700	S. Moss, R. Sawyer, L. Magana	24.2	
T02	02:37:30	02:47:30	30.328259	-99.110269	650	P. Hinton, Y. Hernandez	21.3	
T03	02:37:30	02:47:31	30.086869	-100.370059	700	M. Skrutskie, K. Valenzuela	15.7	
T04	02:38:38	02:57:45	30.088153	-100.096969	732	A. Rolfsmeier, G. Kayl, C. Moczygembra	12.1	
T05	02:37:35	02:47:36	29.948207	-100.761428	539	A. Verbiscer, M. Stothoff, S. Stothoff	7.9	
T06	02:37:30	02:47:30	29.937001	-100.539211	530	R. Smith, R. Williams, B. Hill	3.8	
T07	02:37:31	02:47:31	29.796111	-101.223333	487	J. Jewell, C. Koers, R. Frankenberger	-0.2	
T08	02:37:30	02:47:32	29.765827	-101.128689	511	K. Getrost, R. Karohl	-4.4	
T09	02:37:30	02:47:32	29.695594	-101.318869	420	B. Keeney, J. Kammer	-8.5	
T10	02:37:56	02:47:56	29.680555	-101.172500	466	C. Olkin, J. Hernandez	-11.8	
T11	02:37:31	02:47:33	29.676744	-100.850583	494	J. Keller, H. Levison	-16.6	
T12	02:37:30	02:47:34	29.602608	-101.073395	403	S. Porter, K. Miller, J. Muñoz	-20.6	
T13	02:37:30	02:47:30	29.573468	-100.977743	354	J. Samaniego, S. Kester, R. Cardenas	-24.7	
T14	02:37:30	02:46:30	29.609710	-100.452349	512	J. Dunham, M. Hickinbotham	-28.3	
T15	02:37:34	02:47:36	29.492727	-100.907736	344	D. Dunham, M. Young, R. Mellen	-33.3	
T16	02:37:30	02:47:30	29.449299	-100.951760	354	A. Olsen, R. Bobick	-36.8	
T17	02:37:01	02:47:01	29.437425	-100.738807	346	J. Moore, J. Eaccarino, N. Chevalier	-40.8	
T18	02:37:30	02:48:02	29.374022	-100.878779	296	W. Hanna, J. Salazar, D. Wagoner	-44.9	
T19	02:37:32	02:47:33	29.422104	-100.261023	412	P. Tamblyn, B. Hillard, T. Hillard	-48.7	
T20	02:37:00	02:47:02	29.368826	-100.324983	403	J. Salmon, L. Fuller, T. Hilgendorf	-52.9	
T21	02:37:33	02:47:36	29.252565	-100.539872	332	T. Finley, R. McKnight, R. Rickerson	-56.7	
T22	29.602595	-98.425989	273	B. Tobias, H. Davidson, K. Kotara, R. Tarbell	-61.1	Did not record owing to clouds
T00	02:37:30	02:47:30	29.220583	-100.488628	306	M. Buie, S. Kroll	-64.8	

Note. All times are on 2018 November 18. All site locations are referenced to the WGS84 datum. Offset is the distance perpendicular to the centerline of the last pre-event prediction.

object depending on the weighting used and thus can strongly impact the results of an occultation deployment.

The recommendation for deployment locations of the observing stations was a spacing of 25–30 km centered about the predicted centerline. Had that plan been followed, it is quite likely that both stations would have observed the occultation. However, there were significant logistical constraints for the

deployment locations, and reaching the desired site placements was not possible. These constraints led to the decision to put station S01 on the predicted centerline and live with the slightly nonoptimal location for station S02.

Data from both stations were obtained with the Unistellar eVscope systems. An eVscope is a system based on a 11.4 cm Newtonian-like telescope with an integrated IMX224 CMOS

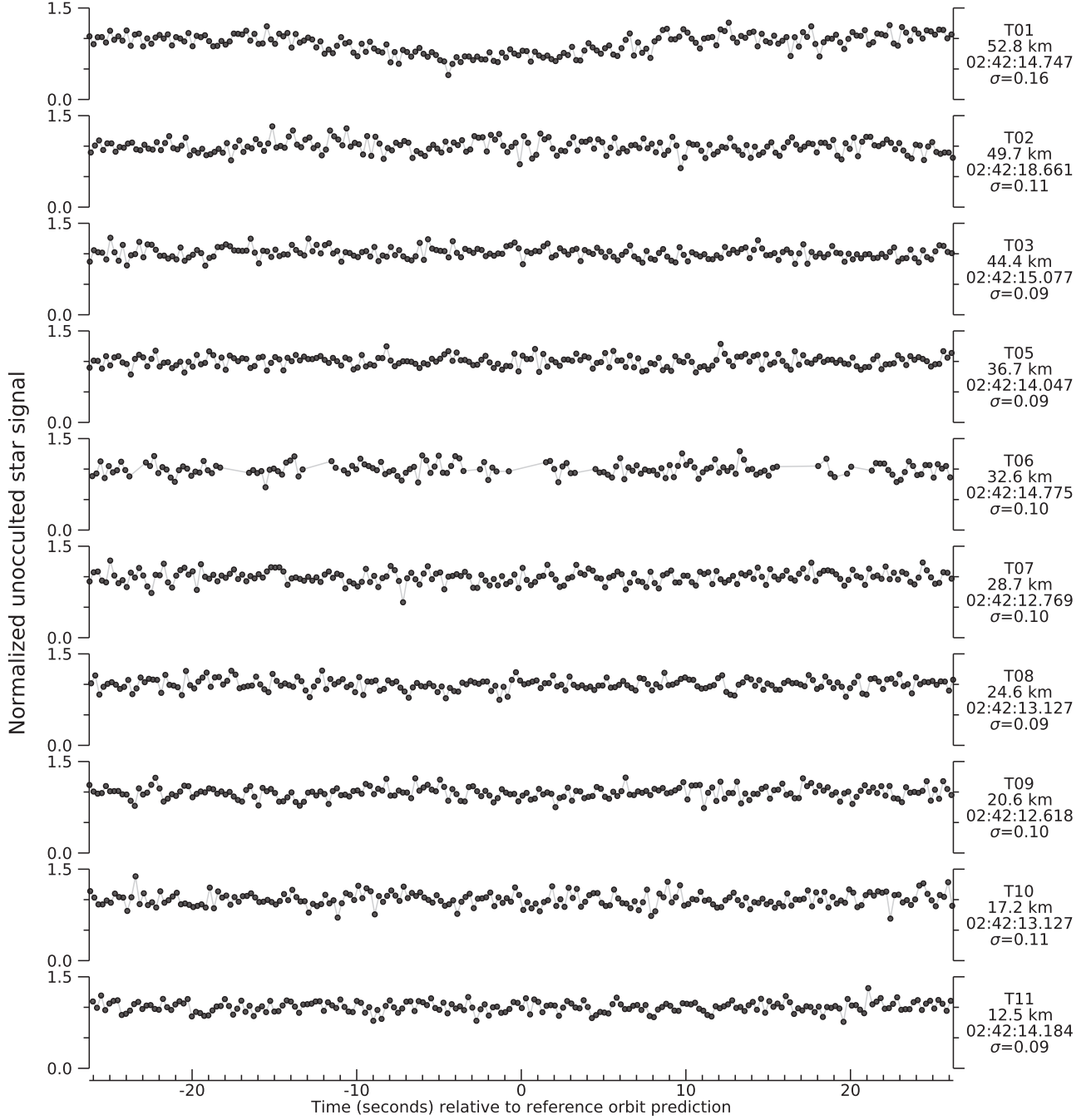


Figure 9. Light curves for LE20181118, part 1. The plots are clipped at 0 and 1.5 for clarity. The labels on the right identify the team, the cross-track offset relative to the final prediction, the reference mid-time, and the standard deviation of the per-point scatter. For those events with a positive detection, the occultation model (in red) is shown as well. The data used for the figure (without clipping) are provided in electronic form.

(The data used to create this figure are available.)

detector and onboard computer for telescope control and data collection; see Marchis et al. (2020) for a full description. Absolute timing of the observations is supported by time information provided by a connected cellular telephone during data collection with an absolute timing accuracy estimated at 50 ms. These observations were further supported by the use of an auxiliary timing system (known as ChronoFlash) that is estimated to improve the absolute timing to a level similar to the QHY174 cameras. The site details and results are given in Table 9. The S01 data used an exposure time of 1 s, and the

S02 data used an exposure time of 0.25 s. The light curves are shown in Figure 13. The data from site S01 show a feature consistent with an occultation. The level during the occultation should drop to zero since Orus was nearly six magnitudes fainter than the star but the observed level is at roughly 30% of the unocculted level, thus ruling out a detection of Orus during the event. It is possible that the target star is actually two closely spaced sources and the S01 data recorded the occultation of one component. The data from S02 do not appear to record an occultation, but there is a possibility of a

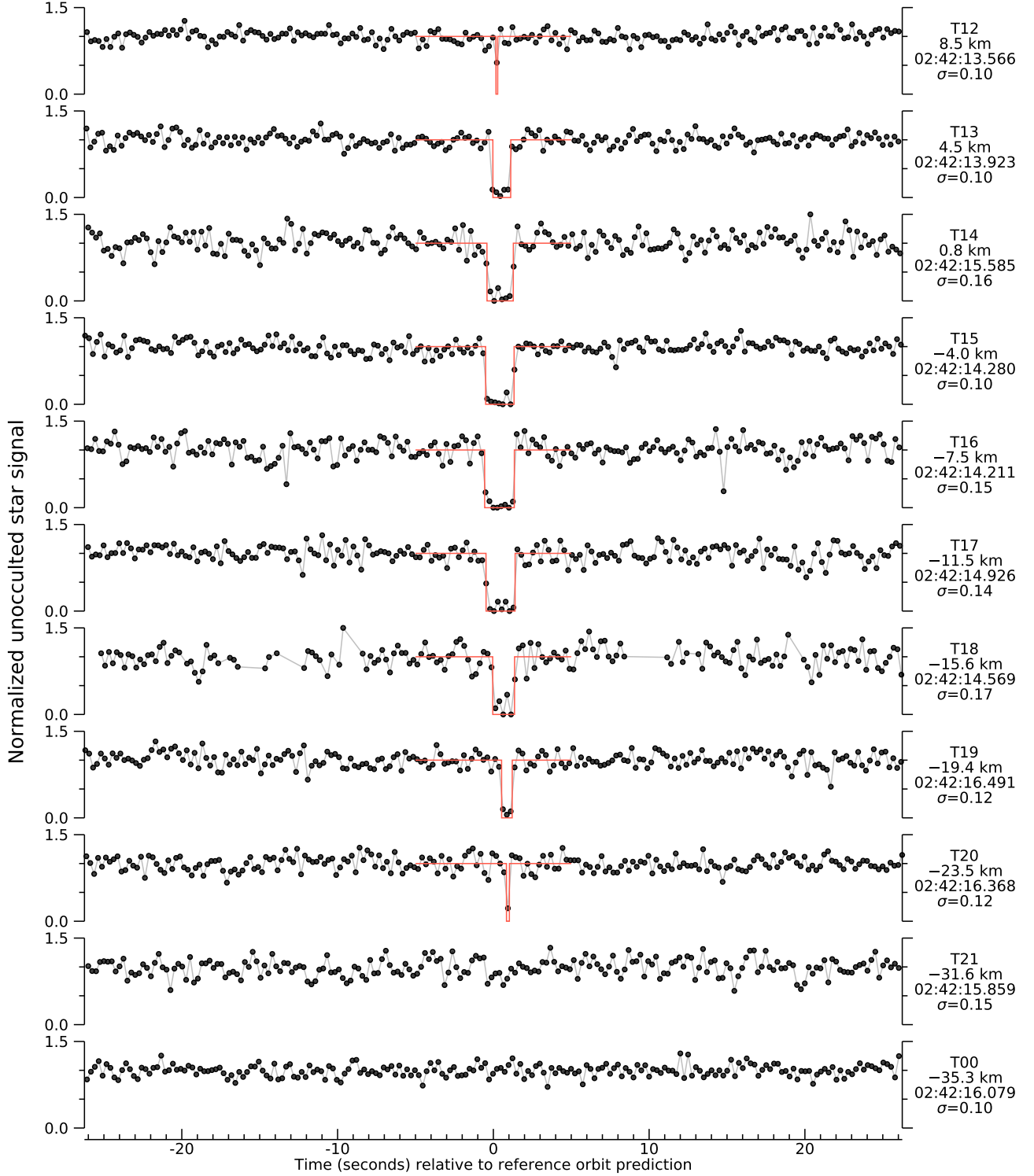


Figure 10. Light curves for LE20181118, part 2. The plots are clipped at 0 and 1.5 for clarity. The labels on the right identify the team, the cross-track offset relative to the final prediction, the reference mid-time, and the standard deviation of the per-point scatter. For those events with a positive detection, the occultation model (in red) is shown as well. The data used for the figure (without clipping) are provided in electronic form.

(The data used to create this figure are available.)

short, grazing event on the other stellar component at +2 s. The dip to zero at +3.5 s is attributed to noise (similar to the dip at -25 s). We do not have sufficient data at this point to completely understand this observation, and some caution is warranted in the interpretation of our derived results. The

following analysis and interpretation are based on the following assumptions: there is only one source and the model occultation baseline goes to zero for the S01 data, and there is no event recorded at S02. The chord length was 4.0 ± 0.7 s for the S01 detection. The uncertainties given are derived from

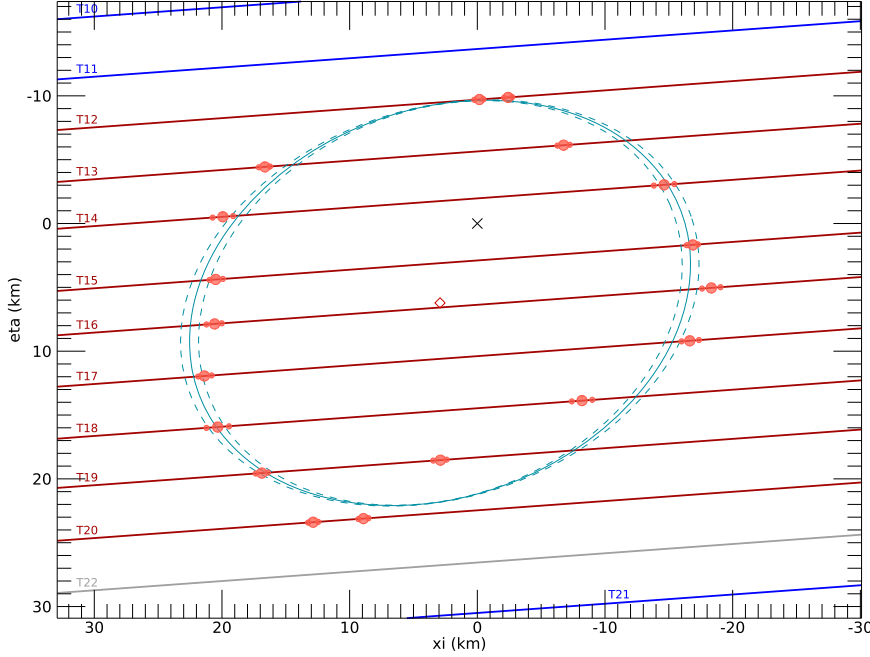


Figure 11. Limb profile for LE20181118. Shadow plane projection of occultation timing. These are tangent plane positions oriented as if looking down on the projected shadow as it would appear on the surface of Earth (see Appendix A for details). Orange circles are the measurements from Table 8; their individual (ξ, η) values are available in a machine-readable format (Table 17). The 1σ uncertainties, when visible, appear as half-size circles. The labeled lines show the track of the star across the object as seen at each site. Orange lines correspond to sites with positive detections, blue lines correspond to sites with negative constraints, and gray lines indicate sites unable to collect useful data. The cross indicates the predicted center based on the final orbit estimate. The diamond symbol indicates the center of the fitted ellipse.

Table 8
Occultation Timings for LE20181118

Team ID	UT Disappearance	UT Reappearance	Length (km)	Offset (km)
T12	02:42:13.733 ± 0.017	02:42:13.846 ± 0.017	2.4 ± 0.5	-0.4
T13	02:42:13.774 ± 0.023	02:42:14.957 ± 0.023	24.2 ± 0.7	-4.4
T14	02:42:15.173 ± 0.039	02:42:16.866 ± 0.039	34.7 ± 1.1	-8.1
T15	02:42:13.783 ± 0.022	02:42:15.612 ± 0.026	37.5 ± 0.7	-13.0
T16	02:42:13.650 ± 0.036	02:42:15.556 ± 0.029	39.1 ± 1.0	-16.5
T17	02:42:14.457 ± 0.035	02:42:16.320 ± 0.026	38.3 ± 0.9	-20.5
T18	02:42:14.527 ± 0.039	02:42:15.928 ± 0.043	28.6 ± 1.2	-24.6
T19	02:42:17.019 ± 0.026	02:42:17.702 ± 0.025	14.0 ± 0.7	-28.5
T20	02:42:17.206 ± 0.020	02:42:17.400 ± 0.020	4.1 ± 0.6	-32.7

Note. All times are on 2018 November 18. Offset is the distance perpendicular to the centerline of the last pre-event prediction. T12 times can be systematically up to 68 ms either earlier or later. T20 times can be systematically up to 28 ms either earlier or later.

the internal random errors in the data and our assumptions. The shadow velocity for this event was 13.7 km s^{-1} ; thus, the chord length was $54.8 \pm 1.0 \text{ km}$. The absolute magnitude we used for Orus was $H_V = 10.300 \pm 0.007$ (S. Mottola 2021, personal communication). If the object were circular and this were a central chord, then the implied albedo would be $p_V = 0.046$. This albedo does indicate a dark object but is not a definitive measurement. We have treated this observation as a central chord for purposes of extracting astrometry (see Table 19). It was clear from the success of the event that the prediction was good, giving us some validation of our weighting scheme for orbit estimation. This astrometry and the albedo will be further improved after a multichord occultation is obtained.

The length of the single chord and the spacing between the two stations are inconsistent with a circular profile if the chord crossed the center of the object. The diameter ($D = 42 \text{ km}$) shown in Figure 12 is the largest possible cross-track width that is centered on the predicted centerline and yet misses station

S02. Figure 14 provides a demonstration of the geometric constraints. With only one detection, we cannot determine a size or shape for even idealized limb profiles. However, the two observations place some interesting constraints on Orus and also provide a useful astrometric measurement. This plot shows an ellipse aligned with the shadow motion direction whose major axis matches the duration of the occultation, and the minor axis is set to just miss the S02 track. The major and minor axes are 54.8 and 42.2 km, respectively, with an axial ratio of 1.3:1. The albedo implied by this ellipse is $p_V = 0.060$. A circular profile with a 54.8 km diameter is shown with dotted lines, and it is clear that such a profile is inconsistent with the negative detection from site S02. Unfortunately, this does not rule out a circular profile, and one example is shown with the dashed circle with a 54.8 km diameter displaced 6 km perpendicular to the track that also misses track S02. Further observations are required to determine a shape for Orus, and these observations will provide useful constraints once more

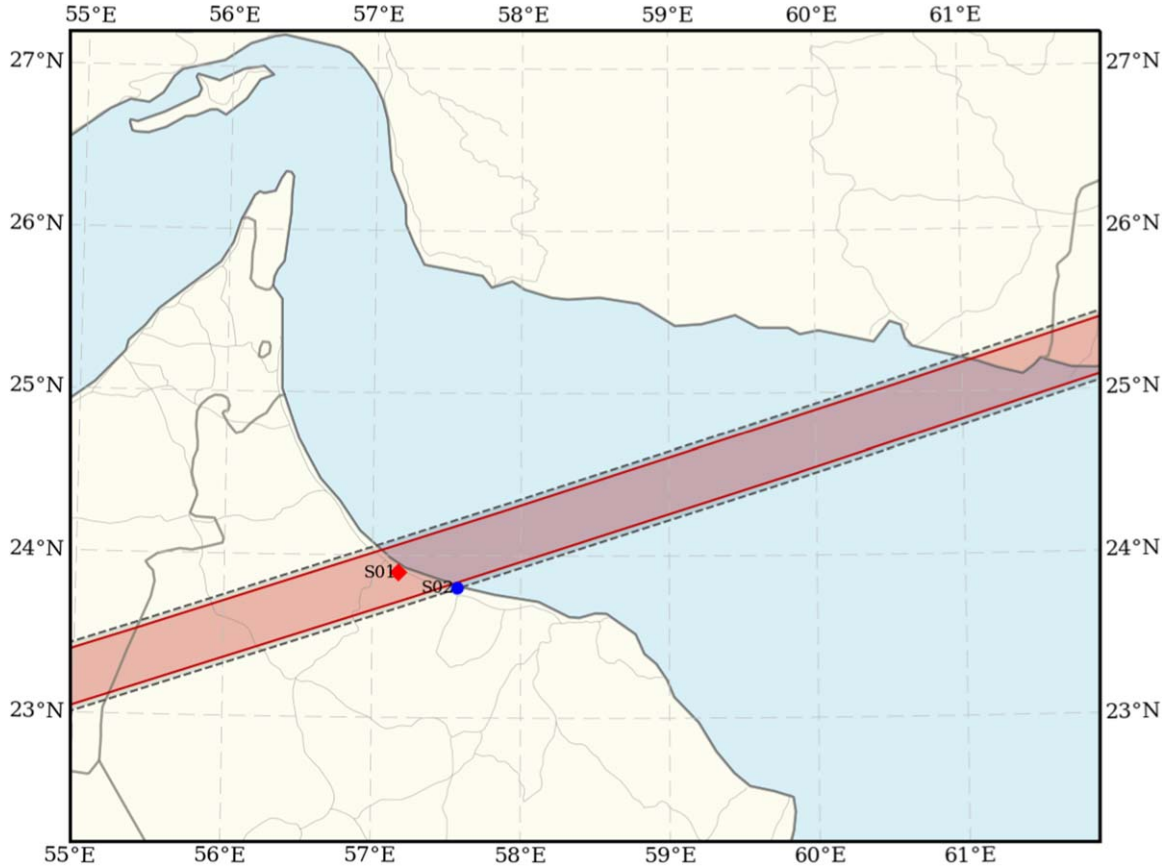


Figure 12. Map of the OR20190907 occultation. The gray region delimited by dashed lines represents the predicted track with a diameter of 51 km. The red shaded region delimited by solid lines shows a notional actual occultation zone with a diameter of 42 km that is consistent with the observations. The observing locations are shown labeled by their site codes. Blue circles indicate good data with no occultation. Red diamonds indicate good data with a positive occultation detection. Faint gray lines show major highways.

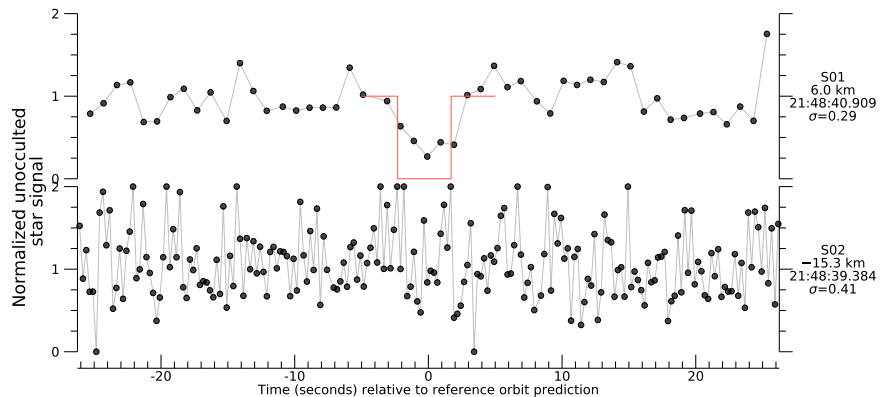


Figure 13. Light curves for OR20190907. The plots are clipped at 0 and 2 for clarity. The labels on the right identify the team, the cross-track offset relative to the final prediction, the reference mid-time, and the standard deviation of the per-point scatter. For the event with a positive detection, the occultation model (in red) is shown as well. The data used for the figure (without clipping) are provided in electronic form.

(The data used to create this figure are available.)

Table 9
Mobile Observing Stations and Teams for 2019 September 7

ID	Lat (deg)	Lon (deg)	Alt (m)	UT Disappearance	UT Reappearance	Observers	Offset (km)
S01	23.890972	57.177278	30	21:48:38.7 ± 0.05	21:48:42.7 ± 0.05	A. Malvache, L. Marfisi	5.3
S02	23.803889	57.568583	25	A. Martin	-16.0

Note. All times are on 2019 September 7. All site locations are referenced to the WGS84 datum. Offset is the distance perpendicular to the centerline of the last pre-event prediction.

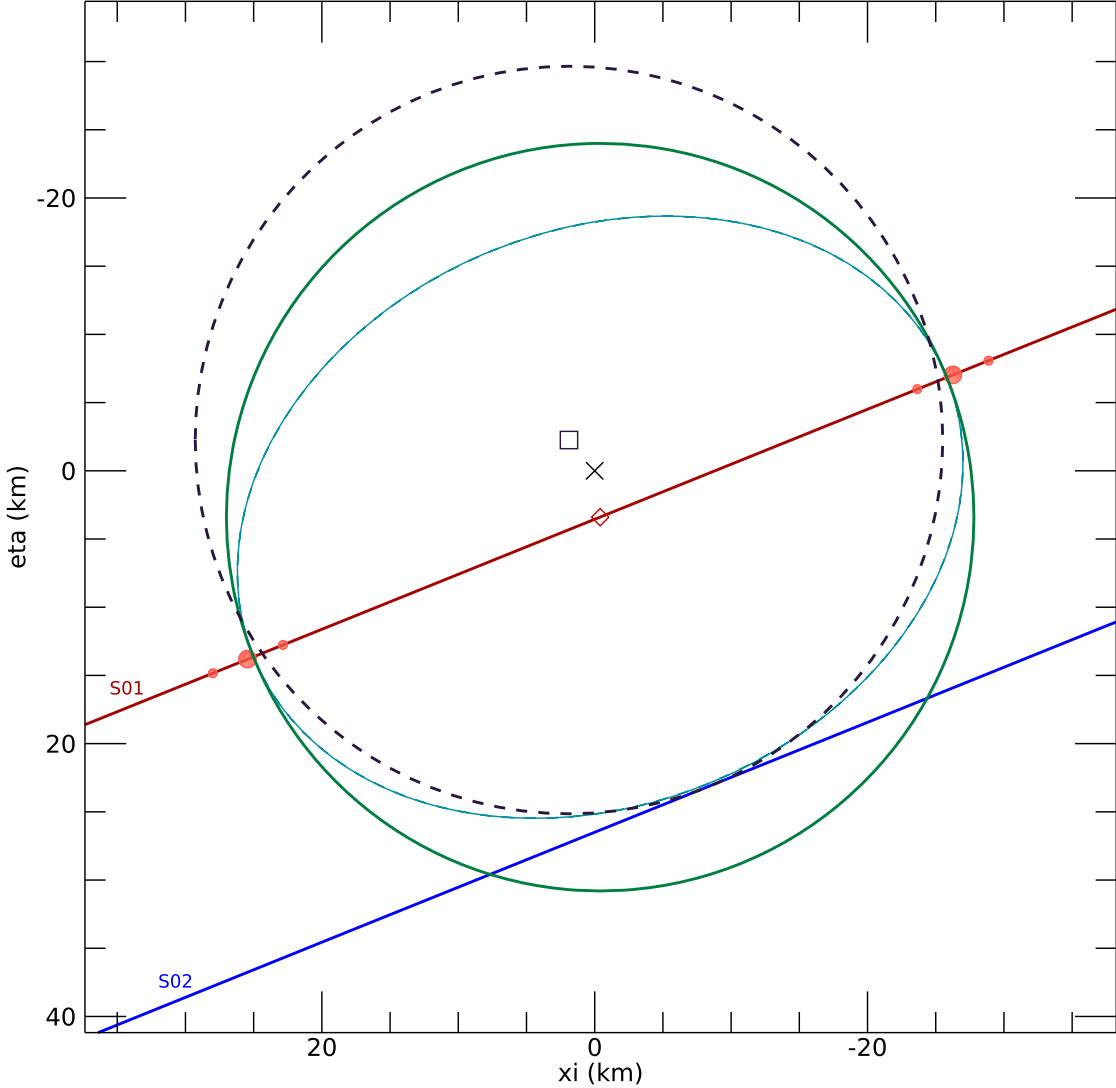


Figure 14. Limb profile constraints for OR20190907 (Orus). This plot diagram shows the shadow plane projection of the occultation timing measurements. These are tangent plane positions oriented as if looking down on the projected shadow as it would appear on the surface of Earth (see Appendix A for details). Orange circles are the measurements from Table 9; their individual (ξ, η) values are available in a machine-readable format (Table 17). The 1σ uncertainties, when visible, appear as half-size circles. The labeled lines show the track of the star across the object as seen at each site. The orange line corresponds to the site with a positive detection, and the blue line corresponds to the site with a negative constraint. The cross indicates the predicted center based on the final orbit estimate. The diamond symbol indicates the center of an ellipse centered on the middle of the chord, aligned with the track direction, and a minor axis that just misses the S02 track with an axial ratio of 1.3:1. For reference, a circular profile (dotted line) is shown with the same center as the ellipse and radius equal to the semimajor axis of the ellipse. The dashed circle has the same radius but is shifted by 6 km, with the center marked by an open square, and also just missed the S02 track.

data are available. These data do provide a useful astrometric positional constraint, and we use these cases to estimate the uncertainty in the astrometry given our assumptions. The absolute timing uncertainty of the data was estimated to be 0.1 s based on the eVscope system timing logs and the performance of the local network timing information. This estimate translates to a down-track uncertainty of 0.4 mas. The cross-track uncertainty is estimated from this figure to be ± 5 km, corresponding to a cross-track error of 1.6 mas, which requires a 1.6 mas offset of the body center from the centerline of the occultation chord. The astrometric position thus derived is 21:15:24.76841, $-06:04:11.4457$ based on the Gaia DR2 catalog position for the target star (see Table 1) for a reference time of 2019 September 7 21:48:40.700 UT for the position of S01 given in Table 9. These uncertainties are not strictly standard deviations from a normal distribution but for now are used as such in our orbit fitting.

6. Event 5—LE20191002

6.1. Prediction

This event was the first for Leucus that used orbit estimates constrained by the prior occultation data. The prediction work for this event was being done in parallel with the Orus event described in the previous section. The positive result from that event provided important confirmation of our prediction methodology. Whenever possible, we used the same methodology and weighting schemes for both Orus and Leucus so that lessons learned from one could be applied to the other. For this Leucus event it appeared that the largest uncertainty in the prediction was in the projected cross-track size of the body. After adding the 2018 occultations, the 1σ uncertainty from the orbit estimate and star position had dropped to 2 km. The two prior events had cross-track dimensions that differed by only 1.2 km, but we still had no good shape and pole constraints to

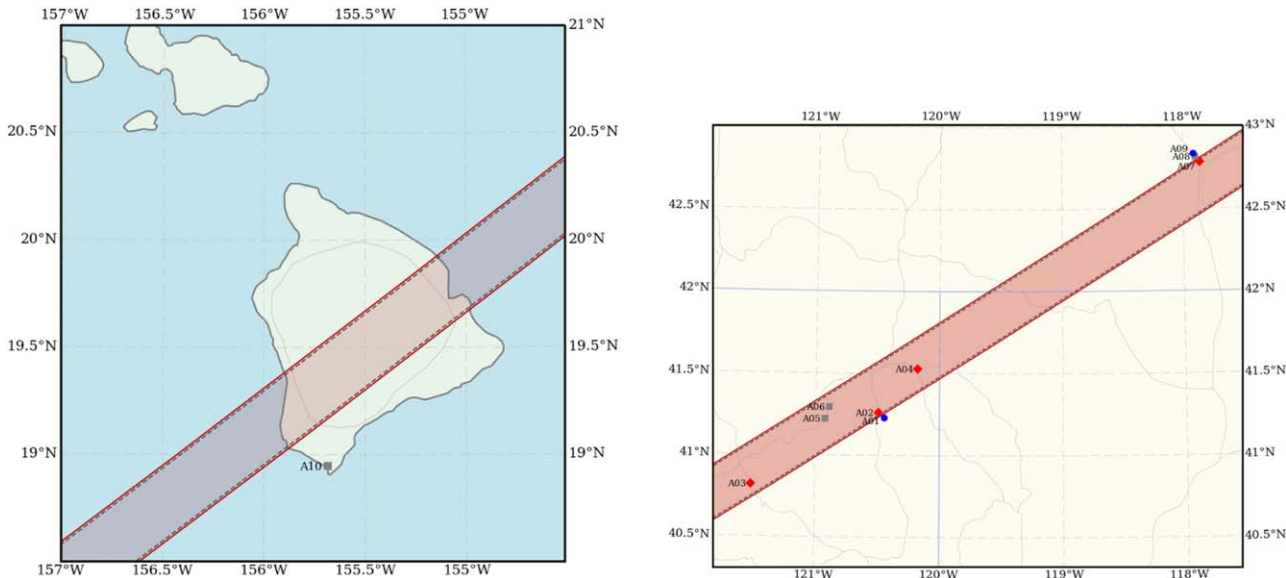


Figure 15. Maps of the LE20191002 occultation. The gray region delimited by dashed lines represents the predicted track with a notional diameter of 30 km. The red shaded region delimited by solid lines shows the actual occultation zone. The observing locations are shown labeled by their site codes. Blue circles indicate good data with no occultation. Red diamonds indicate good data with a positive occultation detection. Gray squares indicate sites unable to collect useful data. Faint gray lines show major highways.

guide the deployment. However, it did appear that our past experience in using a diameter of 45 km was consistently too large. For this event, we used a diameter of 30 km for the prediction.

6.2. Deployment

The location of the predicted shadow path, directly over the western United States, as well as Hawaii, made this event easier to pursue. Figure 15 shows the predicted path and the locations of the observing stations. Table 10 gives the detailed information on all the stations. Due to budget constraints, the Lucy project decided to not pursue a deployment at the same scale as our first two efforts and evaluated other options. Given the location of the predicted shadow path, we decided to involve RECON teams and reach out to the general amateur occultation community to chase this event. Nominally, RECON is a vast stationary network designed to measure occultations with large uncertainties at a low spatial resolution (Buie & Keller 2016). The highly targeted dense mobile deployment necessitated by the low-uncertainty prediction for this event was a methodology that had never been tested using the RECON network; for this reason, beyond the scientific interest in an occultation profile of Leucus, this deployment served as a proof of concept for the effectiveness of the RECON network in this brand new, yet-untested operating mode. The majority of the effort on this event came from RECON, but we were also joined by one team in Hawaii.

A subset of the RECON teams from Northern Oregon through Central Nevada volunteered to transport telescopes and observers from their hometowns to locations across the $\pm 3\sigma$ range of the predicted path. Active in this deployment were small groups from the Gardnerville, NV, Reno, NV, Klamath Falls, OR, Chiloquin, OR, Burney, CA, and Cedarville, CA, RECON teams. In addition, a large group of observers from Sisters High School in Sisters, OR, consisting of nine students and three adults, deployed three telescopes across the northernmost part of the predicted path. Some of these sites, such as

Cedarville and Burney, were able to observe near their homes, while other teams had to travel much farther. The most logically complicated facet of this campaign was the deployment of the group from Sisters, who made an overnight class trip out of the campaign. In the week leading up to the event, this team had to collect equipment from other nearby nonparticipating teams for their deployment efforts.

The deployment plan was built around the nine RECON teams that were tightly coordinated. The 10th team in Hawaii was left to observe from any location they could without any concern for duplication. The prediction was changing right up to the last day, and the RECON teams were more able to adapt to changing locations and last-minute updates. The spacing for the teams was fixed at 5 km. The choice of spacing and the number of coordinated stations had to be balanced against the coverage of the ground track. This decision was supported by the use of a Monte Carlo event simulator (`eventprob.pro` from the Buie IDL library²⁷) that was first used by Buie et al. (2020) and further refined for this project. For this event, we used a circular profile with a 30 km diameter to represent the object. For this size and a random error of just 2 km, the expected outcome was an 85% chance of five chords and a 15% chance of six chords, with the two sites on the outer edges having no chance to see an event. Since the size really was not known, there is another component of error not captured by this simple calculation. A new option was added to include a systematic error term. A strategically meaningful model for the size seemed difficult to quantify with any level of confidence. The simple approach we chose was to add an extra level of uniform random noise to the position of the centerline, where the noise level chosen is the total interval centered on the nominal centerline. The amount of noise can be set to match the degree of conservatism desired while working with a number that has some intuitive value. This approach diminishes the value of computed probabilities of how many chords would be obtained, but as long as that number is comfortably high, this

²⁷ <http://www.boulder.swri.edu/~buie/idl>

Table 10
Mobile Observing Stations and Teams for 2019 October 2

ID	UT Start	UT End	Lat (deg)	Lon (deg)	Alt (m)	Observers	Offset (km)	Comment
A09	07:13:10	07:18:00	42.835543	-117.916795	1197	R. Moorehead, C. Lundgren, C. Fredland, R. Schar	34.6	Images out of focus, data still usable Recording terminated early Did not align on field in time Did not align on field in time Did not record owing to extreme winds
A08	07:13:41	07:14:17	42.815668	-117.897978	1225	D. McCrystal, H. Werts, C. Chapman, T. Ast	32.1	
A07	07:14:21	07:18:00	42.782783	-117.859437	1205	M. Riehle, O. Newton, R. Givot, Z. Lorusso	27.6	
A06	41.222404	-120.925770	1289	S. Anthony, E. Tibay	22.4	
A05	41.291802	-120.889739	1404	J. Kochenderfer	17.8	
A04	07:13:32	07:18:14	41.529037	-120.177122	1434	T. Miller, D. Schulz, B. Cain	12.9	
A03	07:13:42	07:18:31	40.819070	-121.513590	1008	M. von Schalscha	7.6	
A02	07:14:35	07:18:25	41.261313	-120.494285	1401	T. Stoffel, J. Rigby	2.8	
A01	07:13:21	07:18:22	41.228707	-120.446183	1404	J. Bardecker	-2.2	
A10	18.946398	-155.683690	38	C. Erickson	-13.9	

Note. All times are on 2019 October 2. All site locations are referenced to the WGS84 datum. Offset is the distance perpendicular to the centerline of the last pre-event prediction.

issue is not a driving consideration. A set of bounding cases for the systematic error were developed. The most compact case that was deemed reasonable was 2 km random error with an additional 5 km of systematic error and seemed to be comparable to the variation we might expect in the projected track width due to the shape and aspect of the object. The upper bounding case we chose was a spacing of 6 km, a random error of 2 km, and a systematic error of 30 km. The compact case still formally precluded the edge of the object being outside the deployment region, meaning that the outermost two stations had no chance of seeing an occultation. The bounding case had the same expected outcome but with on average one less chord expected than the compact case. Framed this way, the only real choice was in the station spacing. The deciding factor was seeing that for a 5 km spacing and 30 km systematic error, the probability of the outermost stations seeing an event was about 8%. This meant that the worst outcome expected was to not get one of the bounding chords outside the body but the overall coverage would still be very good. Guided by this analysis, we chose a 5 km track spacing centered on the predicted centerline. A table of the deployed stations is provided (Table 10).

6.3. Observations

All teams successfully deployed on or near their assigned track. The track spacing was 5 km, thus covering 36 km across the predicted path, with each team asked to set up within 250 m of their assigned track. At the time of the event, the skies were clear and calm for the RECON teams. Two of the three stations deployed by the Sisters team (A07–A09) successfully collected data for this event. One station (A08) was set up and recording on the target field, but the recording was terminated prematurely. The team reported that no occultation was seen visually. Both of the stations deployed by the Klamath Falls (A05) and Chiloquin (A06) team experienced difficulties aligning the telescopes and did not record the field on time. The remaining four stations were able to successfully collect data for this event. In total, six out of the nine RECON stations recorded usable data. Of these six, four recorded a positive detection and two recorded clear misses. Eight of the RECON teams observed with the standard RECON equipment: a Celestron CPC1100 with a MallinCAM video camera (Buie & Keller 2016). Station A01 observed using a 20 cm telescope and a Watec 910HX/RC video camera. The 10th team in Hawaii was unable to record data owing to high winds on the south side of the island. This experience provided an important lesson on the need for more practice sessions leading up to events of this type. This was a known risk going into the deployment and invaluable information for planning future events.

6.4. Photometric Analysis

The RECON teams use analog video recording equipment as described in Buie & Keller (2016). The data processing is described in more detail elsewhere (Buie et al. 2018, 2020; Leiva et al. 2020). All teams used a SENSEUP setting of 32, or roughly an integration time of 0.5 s, with the exception of A01, which used an integration of 16 \times , or roughly 0.25 s. The precise timing comes from an IOTA-VTI GPS device that timestamps the video images. Aperture photometry of the target star and on-chip comparisons are used to extract occultation light curves.

Most of the RECON videos were very clean, were in focus, and needed no special handling to extract clear light curves with good S/N. The exception was station A09, where the team ran out of time and as a result did not reach proper focus and did not use the correct integration factor (64X instead of the target value of 32X). However, the longer exposure time partially compensated for the poor focus, and it was possible to extract a light curve with a decent S/N of 3.9—sufficient to confirm a nondetection for this site, though at a lower time resolution than desired. The final light curves are shown in Figure 16.

6.5. Result

The extracted occultation timing measurements are listed in Table 11. Even though the coverage density was not as high for this campaign as for the events in 2018, the occultation detections are still detailed enough to show a clearly non-elliptical profile. The three northernmost detections in Figure 16 are consistent with a simple ellipse, but the southernmost chord from A02 requires the shape to have a significant departure from elliptical. The A02 chord length is short at 7.4 km, while the next chord just 4.8 km north is 44.1 km long. Also, the center of the A02 chord is shifted compared to the center of the A03 chord. The final geometry is shown in Figure 17 with an elliptical profile overlaid. This elliptical fit does not match the A02 chord well at all. The length of A02 is much shorter than A03, its closest neighbor. Similar to the earlier events, a large depression or facet seems to be required on the southern end of the object. The limits on the cross-track size are not quite as tight as the other campaigns. The size must be larger than 24.8 km and must be less than 36.8 km, but neither of these limits is particularly constraining. However, it is interesting to note that the cross-track size of the fitted ellipse is 32 km, which is very consistent with the other events. Also note that the shallow and broad dip before the occultation in the A04 light curve is due to a brief moment of much worse seeing, and its effects could not be completely removed during calibration.

7. Event 6—OR20191104, an Astrometric Lesson Learned

Discussion of this event is included owing to its impact on the prediction process and reaching a deeper level of understanding of our own astrometry. On 2019 November 4, a star was to be occulted by Orus and visible from north-central Australia, just south of Darwin. We deployed a large team for this event. All practice nights were usable, but on the night of the event there were widespread heavy clouds and no useful observations were possible.

Much of the details of the final end state of our astrometric data processing can be found in Appendix B, but the final breakthrough in understanding came during the prediction work for this event. Following the success of the OR20190907 event, we anticipated that we had an accurate prediction for this event. Our process was further confirmed by the success with LE20191002. We had been running cross-checks of our orbit estimates against those provided by JPL, and everything seemed to be consistent. A series of weekly updates was begun on the orbit estimation and the resulting occultation prediction, including the uncertainty in the ground track. Our robotic telescope system (see Appendix B) was observing Orus and Leucus every night that the Moon was more than 30° away.

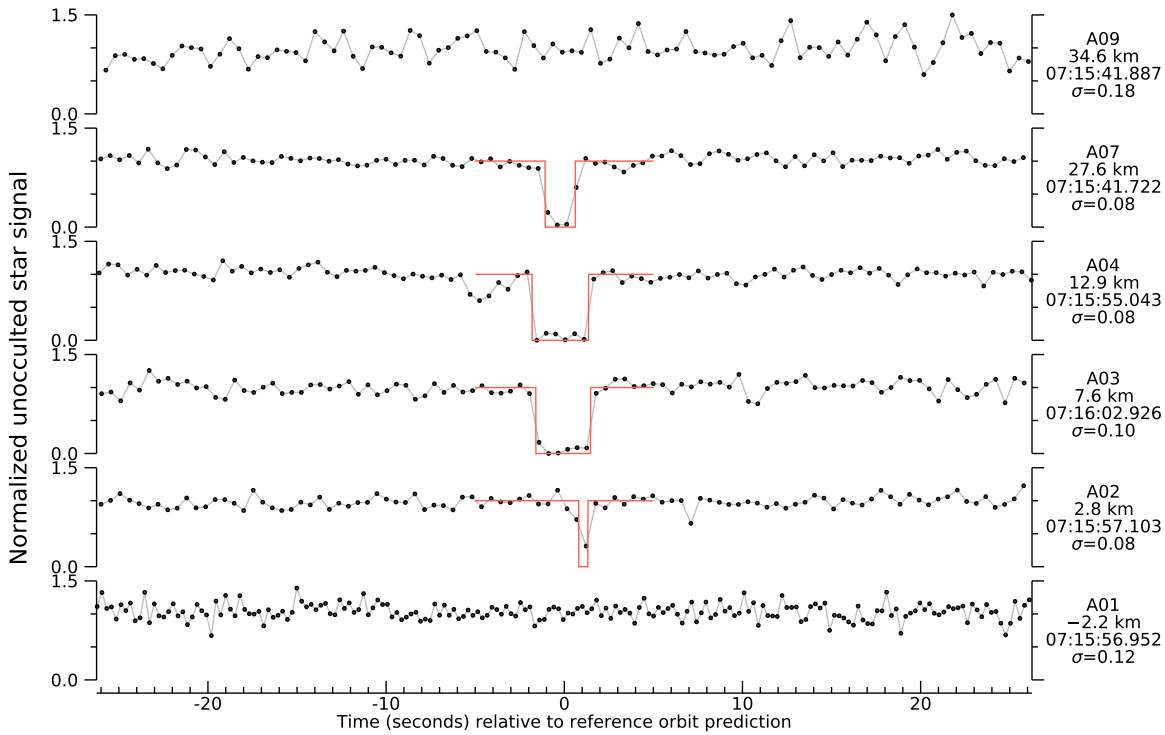


Figure 16. Light curves for LE20191002. The plots are clipped at 0 and 1.5 for clarity. The labels on the right identify the team, the cross-track offset relative to the final prediction, the reference mid-time, and the standard deviation of the per-point scatter. For those events with a positive detection, the occultation model (in red) is shown as well. The data used for the figure (without clipping) are provided in electronic form.

(The data used to create this figure are available.)

Table 11
Occultation Timings 2019 October 2

Team ID	UT Disappearance	UT Reappearance	Length (km)	Offset (km)
A07	07:15:40.741 ± 0.041	07:15:42.377 ± 0.041	24.3 ± 0.8	27.6
A04	07:15:53.392 ± 0.018	07:15:56.254 ± 0.025	45.9 ± 0.6	12.9
A03	07:16:01.441 ± 0.053	07:16:04.270 ± 0.045	44.1 ± 0.4	7.6
A02	07:15:57.840 ± 0.044	07:15:58.365 ± 0.045	7.4 ± 0.9	2.8

Note. All times are on 2019 October 2. Offset is the distance perpendicular to the centerline of the last pre-event prediction.

Table 12 summarizes the astrometric data collected on Orus for this project, and Table 13 summarizes the Leucus effort.

The predictions for both OR20191104 and LE20191229 were being worked at the same time. As new robotic telescope data came in, we updated the orbit estimates and the resulting predictions. The four occultation-based positions for Leucus and the position for the one Orus event provided very strong constraints. During the time leading up to this event, it was a continuing challenge to keep the Leucus and Orus orbits consistent with the occultation position. As we added more data each week, this difficulty continued to grow until there was nothing that could be done to reconcile all the data sets. This problem manifested in seeing a monotonic creep of the predicted shadow northward with each new week of data added. The change from one week to the next was always within the formal uncertainties, but looking across all predictions over time, we came to the conclusion that some systematic error was pulling the orbit off of true. In the final days before the Orus campaign, we pursued the idea that refraction was systematically affecting the astrometry. The full

details of what we learned and the correction needed are provided in Appendix B. We learned that the differential refraction between the target (either Orus or Leucus) and the field stars was adding a small but significant shift to the data. Given that the data closest to the time of the occultations were coming from the robotic telescopes, it seemed reasonable to conclude that they were effectively gaining weight as event time approached. Once the refraction correction was added, the data were much more consistent. Unfortunately, we were unable to confirm these theories with the Orus event itself, but they were crucial to the success of the next event.

8. Event 7—LE20191229

8.1. Prediction

Once the problem with the astrometry was solved for the previous Orus event, our prediction process proceeded very smoothly. By this time, the observing season was drawing to a close, and fewer and fewer data were coming in each week. As a result, the updates to the predictions in the last weeks before

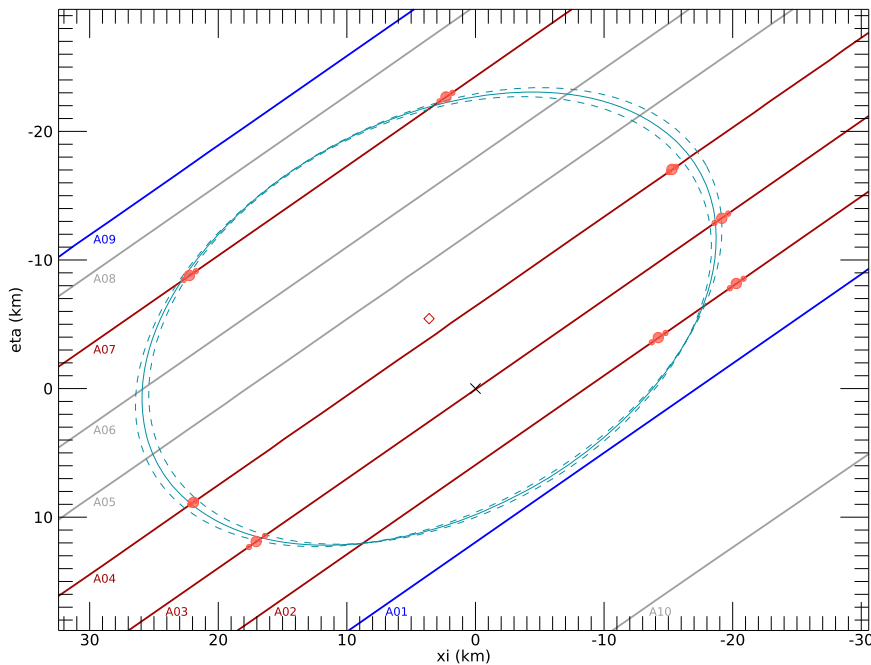


Figure 17. Limb profile for LE20191002. Shadow plane projection of occultation timing. These are tangent plane positions oriented as if looking down on the projected shadow as it would appear on the surface of Earth (see Appendix A for details). Orange circles are the measurements from Table 11; their individual (ξ, η) values are available in a machine-readable format (Table 17). The 1σ uncertainties, when visible, appear as half-size circles. The labeled lines show the track of the star across the object as seen at each site. Orange lines correspond to sites with positive detections, blue lines correspond to sites with negative constraints, and gray lines indicate sites unable to collect useful data. The cross indicates the predicted center based on the final orbit estimate. The diamond symbol indicates the center of the fitted ellipse. The chord for A02 is much shorter than the ellipse fit suggests. See text for details.

Table 12
Robotic Astrometry Summary for Orus

Cutoff Date	MN	MO	CO	Comments
2018-08-31	5	116	116	...
2018-09-30	11	226	342	...
2018-11-30	1	4	346	...
2019-05-31	1	4	350	...
2019-06-30	1	4	354	...
2019-07-31	14	189	543	...
2019-08-27	19	489	1032	OR20190907 predict
2019-08-31	22	504	1047	
2019-09-30	20	110	1157	
2019-10-31	14	98	1255	OR20191104 predict
2019-11-24	11	41	1296	Last orbit fit
2019-12-21	4	4	1300	...

Note. MN—number of nights of data. MO—number of measurements in that month. CO—cumulative number of measurements up to cutoff date. The complete, point-by-point data set is available in a machine-readable format. (This table is available in its entirety in machine-readable form.)

the event were smaller than the size of the shadow and not systematically drifting. This situation greatly simplified the deployment process, as it allowed the teams to conduct advanced scouting on observing locations. The final prediction is represented by the gray region shown in Figure 18.

8.2. Deployment

The deployment for this event was a collaboration between the Lucy project and several organizations. Lucy provided 10 20 cm SkyWatcher telescopes, procured for the OR20191104 deployment (Section 7) but otherwise the same as described in

Table 13
Robotic Astrometry Summary for Leucus

Cutoff Date	MN	MO	CO
2018-07-31	5	52	52
2018-08-31	15	331	383
2018-09-30	5	100	483
2019-07-31	4	69	552
2019-08-31	4	27	579
2019-09-30	22	110	689
2019-10-31	14	70	759
2019-11-30	8	37	796

Note. MN—number of nights of data. MO—number of measurements in that month. CO—cumulative number of measurements up to cutoff date. The complete, point-by-point data set is available in a machine-readable format.

(This table is available in its entirety in machine-readable form.)

Buie et al. (2020). Some of the observers participated in the LE20181114 deployment (Section 3) and were already familiar with the equipment. For some, it was their first time using these systems. Two weeks prior to the event were available for practice, and the night before the event was intended to be a dress rehearsal. Unfortunately, the 10 days prior to the event were consistently cloudy and rainy in Phoenix, severely limiting the amount of usable practice time. Inadequate opportunities to practice was a contributing factor for most of the unsuccessful teams.

Supplementing the Lucy (SwRI) equipment were several IOTA teams and individuals using their own equipment and RECON teams from Blythe, CA, Calipatria, CA, and Yuma, AZ, using the same equipment as for the LE20191002 deployment (Section 6). Finally, SETI Institute and Lowell

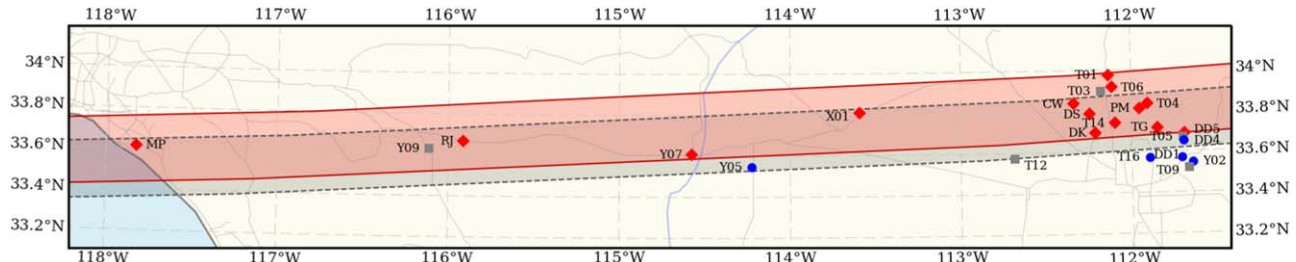


Figure 18. Map of the LE20191229 occultation. The gray region delimited by dashed lines represents the predicted track with a notional diameter of 30 km. The red shaded region delimited by solid lines shows the actual occultation zone. The observing locations are shown labeled by their site codes. Blue circles indicate good data with no occultation. Red diamonds indicate good data with a positive occultation detection. Gray squares indicate sites unable to collect useful data. Faint gray lines show major highways.

Table 14
Mobile Observing Stations and Teams for 2019 December 29

ID	UT Start	UT End	Lat (deg)	Lon (deg)	Alt (m)	Observers	Offset (km)	Comment
T01	03:29:15	03:39:15	33.976167	-112.132610	656	E. Sahr, J. Kidd, W. Wilkinson, M. Wilkinson	23.3	
T06	03:29:03	03:39:03	33.916639	-112.112170	656	T. Blank, P. Yeargain	17.2	
DS3	33.899111	-112.164889	613	D. Stanbridge, Dunham	15.6	Ran out of time for setup
T03	33.897500	-112.180280	541	S. Insana, K. Hollingsworth	15.4	Did not record at correct time
DS2	33.864028	-112.190556	547	D. Stanbridge, Dunham	12.1	Difficulties with setup
X01	03:31:10	03:36:12	33.808501	-113.592125	579	J. Keller, S. Rost, J. Rost	11.3	
CW	03:29:09	03:39:05	33.837870	-112.339800	542	M. Collins, L. Wasserman	9.9	
MP	03:32:02	03:35:01	33.614801	-117.825010	130	F. Marchis, D. Peluso	9.8	
T04	03:28:59	03:38:59	33.833056	-111.906110	762	B. Ewing, M. McClure	8.0	
RJ	03:30:00	03:37:00	33.668989	-115.914789	420	R. Jones	6.5	
PM	03:32:42	03:34:37	33.811905	-111.952215	654	P. Maley	6.0	
DS1	03:33:23	03:33:59	33.786902	-112.245768	1560	D. Stanbridge, Dunham	4.8	
Y09	33.631250	-116.111567	-34	A. McCandless, A. Vazquez, D. Gupton, J. Bustos, M. Garcia	3.3	Data recording failure
T14	03:29:03	03:34:41	33.741028	-112.097770	458	M. Brown, L. Brown	-0.8	Recording terminated early
TG	03:32:11	03:35:10	33.715603	-111.849369	746	T. George	-4.1	
DK	03:33:30	03:34:30	33.694167	-112.212778	400	D. Kenyon	-5.3	
Y07	03:31:13	03:36:12	33.607992	-114.577915	74	N. Patel, D. Barrows	-5.5	
DD5	03:33:32	03:33:49	33.685895	-111.693762	1613	D. Dunham, J. Dunham	-7.3	
T05	03:31:52	03:41:51	33.668417	-111.701720	477	S. Adams	-9.5	On the wrong field
DD4	03:32:34	03:34:24	33.650448	-111.697655	1566	D. Dunham, J. Dunham	-10.9	
Y05	03:30:10	03:36:14	33.547633	-114.227350	339	D. Conway, K. Conway	-13.0	
DD3	33.624306	-111.715278	498	D. Dunham, J. Dunham	-13.9	Data entry error
T12	03:29:00	03:39:00	33.573611	-112.686110	339	W. Hanna, P. Hanna	-16.0	Equipment malfunction
T16	03:29:44	03:39:44	33.570217	-111.896900	333	B. Keeney	-19.0	
DD1	03:32:49	03:34:47	33.567900	-111.710400	463	D. Dunham, J. Dunham	-19.7	
Y02	03:29:00	03:39:00	33.547594	-111.645713	256	K. Getrost	-22.1	
T09	33.519450	-111.670006	403	K. Healy, C.-F. Healy	-24.8	Did not align on field in time

Note. All times are on 2019 December 29. All site locations are referenced to the WGS84 datum. Offset is the distance perpendicular to the centerline of the last predicted event.

Observatory each provided personnel and equipment that contributed to this effort. In all, 24 stations deployed for this event; their details are summarized in Table 14, and the equipment and exposure duration settings are summarized in Table 15. The deployed equipment represents a varied collection of systems and methods. The range of apertures runs from 8 cm up to 41 cm, and the cameras have a roughly equal mix of CMOS framing cameras and older video cameras. All systems provided timing referenced to GPS signals, some with video overlay hardware, some with direct tagging in hardware from the GPS system. The system from Lowell Observatory

(CW) was using a new system under development that required post-processing efforts on the timing but was ultimately referenced to GPS time. The Unistellar eVscope system setup for this event used only the built-in cell-phone-based timing.

On event night, each team went to a location on their assigned track. The intent of our deployment plan was to evenly space out the observing stations from $\pm 3\sigma$ about the predicted track. The choice in the coverage range was driven more by our uncertainty in knowing the profile of the object that we would be seeing rather than where the centerline would be. The deployment locations are shown in Figure 18, along

Table 15
Equipment and Settings for 2019 December 29 Data

ID	Ap (cm)	Camera	ExpTime (s)	Timing	Mount	Notes
T01	20.3	QHY174	200 ms	GPS	TZ	T80, Q1001
T06	20.3	QHY174	200 ms	GPS	TZ	T84, Q1006
DS3	12	RCNEA	...	VTI	PP	
T03	20.3	QHY174	...	GPS	TZ	T81, Q1003
DS2	12	RCNEA	...	VTI	PP	
X01	28.0	QHY174	100 ms	GPS	TZ	R-Searchlight, QX01
CW	23.5	FLIR	100 ms	GPS	GEM	Development system
MP	11.4	UniCam	200 ms	GPS	TZ	eVscope, Chronoflash
T04	20.3	QHY174	200 ms	GPS	TZ	T82, Q1004
RJ	20.3	Wattec 910HX	NTSC 2x	VTI	TZ	
PM	20	Wattec 910HX	NTSC 4x	VTI	TZ	
DS1	12	RCNEA	NTSC 2x	VTI	PP	
Y09	28.0	MallinCAM	...	VTI	TZ	R-Calipatria
T14	20.3	QHY174	200 ms	GPS	TZ	T88, Q1114
TG	30	Wattec 910HX	NTSC 2x	VTI	TZ	
DK	25.4	RCNEA	NTSC 8x	VTI	TZ	
Y07	28.0	MallinCAM	NTSC 4x	VTI	TZ	R-Blythe
DD5	25.0	RCNEA	NTSC 2x	VTI	PP	
T05	20.3	QHY174	200 ms	GPS	TZ	T83, Q1005
DD4	8	Wattec 910HX	NTSC 8x	VTI	PP	
Y05	28.0	MallinCAM	NTSC 4x	VTI	TZ	R-Yuma
DD3	40.6	QHY174	...	GPS	TZ	
T12	20.3	QHY174	200 ms	GPS	TZ	T87, Q1012
T16	20.3	QHY174	200 ms	GPS	TZ	T89, Q1016
DD1	8	Wattec 910HX	NTSC 8x	VTI	PP	
Y02	25.4	QHY174	200 ms	GPS	TZ	
T09	20.3	QHY174	...	GPS	TZ	T85, Q1009

Note. T and Q identifiers are for the SwRI portable systems. R—identifiers are for RECON teams. GEM—German equatorial mount; PP—pre-point system; TZ—alt/az mounts. VTI—video-time inserter (GPS base). GPS means timing directly read and saved with data. NTP—network time protocol. NTSC—indicates video data followed by the field integration factor. RCNEA—RunCam NightEagle Astro. QHY174 are all QHY174M-GPS models. FLIR—FLIR Blackfly 23S6M-C (sensor IMX249).

with the prediction (gray region bounded by dashed lines) and the actual track location and size. The actual shadow path was at the northern end of the range we deployed to and slightly wider than expected. In fact, we did not have a deployed site north of the shadow that could have further pinned down that edge of the object. Even with this caveat, the results from this effort were very good.

8.3. Observations

The light curves for 30 s centered on the predicted mid-time at each station are shown in Figures 19 and 20. Out of 19 stations with good data, 14 of them recorded an occultation. Of these 14, there are three chords that were duplicated almost exactly. While these are instructive for showing agreement between different systems, the duplications were not intended as part of the deployment. However, the full intended cross-track range was covered. Station T01 was expected to be the northernmost chord. In the south there were plenty of stations recording a clear miss, and that end of the object is well covered. The northern end could have used more stations and better coverage up through and slightly beyond T01. The lower bound to the cross-track size of the shadow is 30.6 km. The ellipse fit is consistent with a cross-track size of 35 km.

Looking at Figure 20, the data for station DD4 appear to show a very short dip. If this dip is treated as an occultation, the chord length is roughly 2 km, but the timing would require a rather peculiar and nonphysical spike on the south end of the object. We do not consider this to be a real detection, but it is

unfortunate that the T05 station (midway between DD4 and DD5) was unable to record data to confirm or refute this determination.

The timing extracted from the positive detections can be found in Table 16, along with estimated uncertainties. The chord lengths vary from 9.8 to 47.6 km. Looking at the offsets, we can see that the cross-track projected size of the body was at least 30.6 km. There is no simple upper bound for this event since there were no negative detections north of T01. Based on these offsets, T04 was the site closest to the center of the shadow, and there were five detections to the north and eight detections to the south. This asymmetry in coverage is partially a consequence of the difficulties in coordinating all these stations combined with the changing prediction. The existing tools used by IOTA for coordinating campaigns were never designed for this type of deployment. It remains a challenge to achieve the results from a tightly controlled deployment such as LE20181114 and LE20181118 that can take advantage of the looser confederation of IOTA observers and a corresponding reduction in the coordination effort required. Another aspect of predictions at this precision level is the element of intuition that needs to be applied to the deployment strategy relative to the simple normal distribution description of the likelihood of seeing an event. Ideally, these deployments are based on the decision of the ground-track coverage desired that includes all components of the uncertainty. Then, when the number of stations is known, the spacing of sites can be defined. Note that a uniform spacing of stations is just one possibility for the

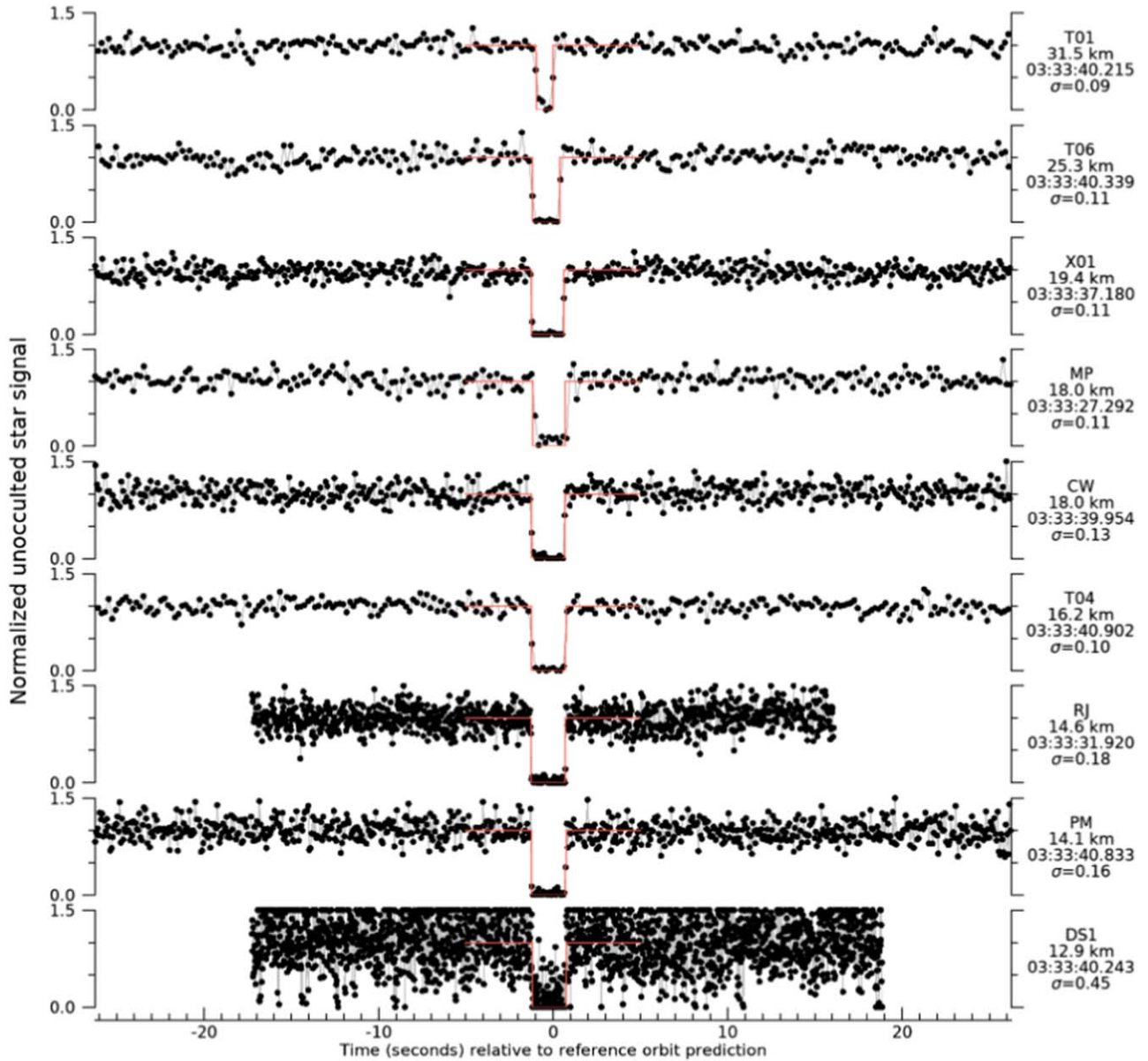


Figure 19. Light curves for LE20191229, part 1. The plots are clipped at 0 and 1.5 for clarity. The labels on the right identify the team, the cross-track offset relative to the final prediction, the reference mid-time, and the standard deviation of the per-point scatter. For those events with a positive detection, the occultation model (in red) is shown as well. The data used for the figure (without clipping) are provided in electronic form.

(The data used to create this figure are available.)

desired spread. Cases can be made for a variable spacing where the near-central chords would be sparser compared to those near the shadow edges. Having a tool that dynamically supports building a deployment plan as late as possible would have definitely helped for this event. Regardless, it is still important to note that the perfect occultation deployment should always have stations that probe outside the shadow on both sides.

8.4. Results

The projected limb profile of Leucus is shown in Figure 21. Once again, we see an outline with strong topographic signatures. The fitted ellipse provides a rough match to the object, and it is especially unfortunate that there were no

additional sites north of site T01. Lacking this information, we do not know if that end of the object is curved similar to what the ellipse would suggest, or if there is an additional projection in that direction. Using the ellipse as a reference “surface,” then there are two relatively sharp positive features at three o’clock and seven to eight o’clock that are a few kilometers high. The southern end shows a negative feature that is a few kilometers deep. The negative departure from the ellipse at one to two o’clock is somewhat bigger at 3–4 km and more abrupt. The ellipse also suggests that this aspect had a 35 km cross-track size, larger than for the other events.

There are three chord pairs in these data: CW/MP, RJ/PM, and DK/Y07. In the latter two cases, the timing agrees to within the measurement uncertainties, with some small

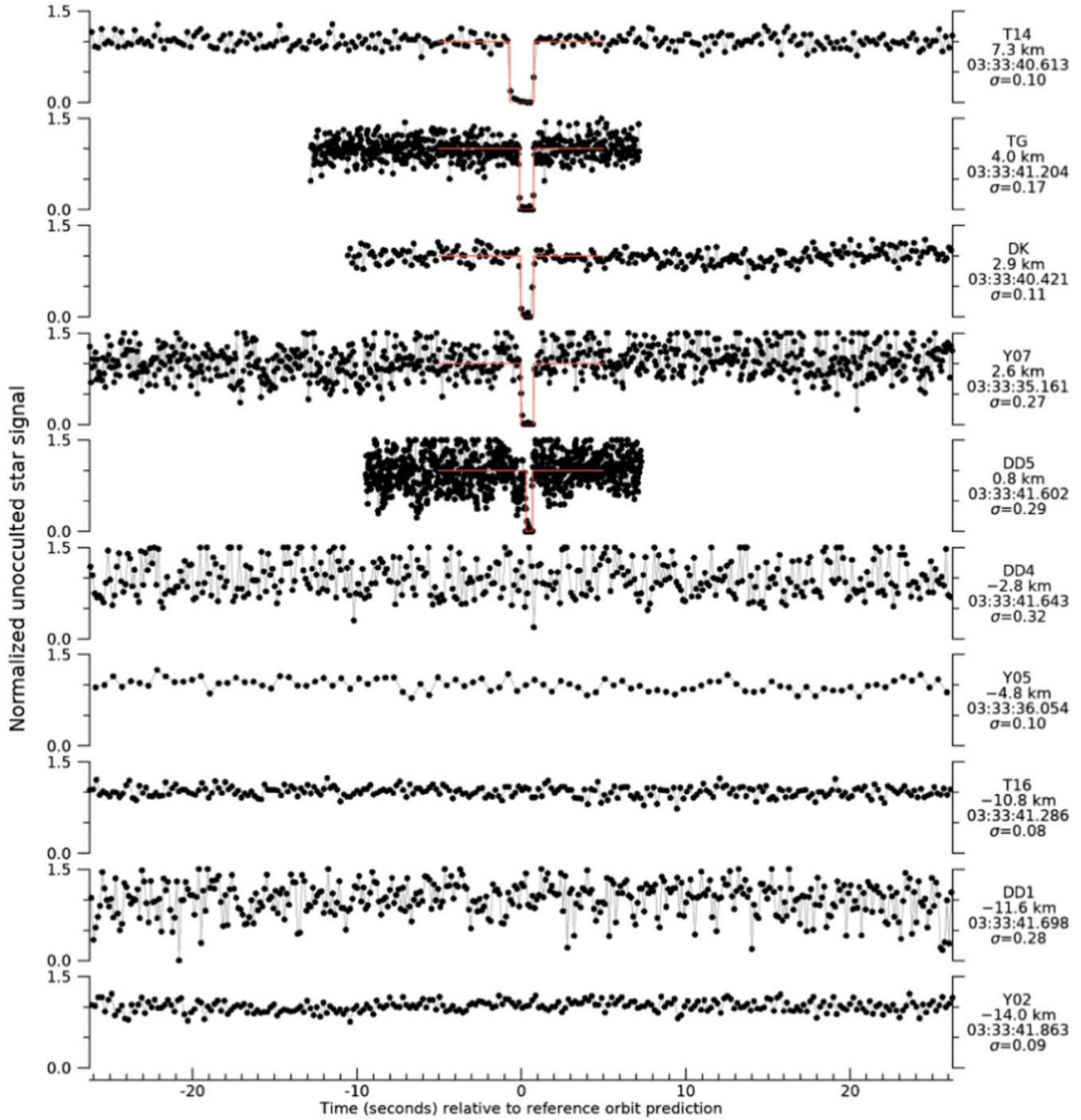


Figure 20. Light curves for LE20191229, part 2. The plots are clipped at 0 and 1.5 for clarity. The labels on the right identify the team, the cross-track offset relative to the final prediction, the reference mid-time, and the standard deviation of the per-point scatter. For those events with a positive detection, the occultation model (in red) is shown as well. The data used for the figure (without clipping) are provided in electronic form.

(The data used to create this figure are available.)

accommodation due to topography. The timing difference between CW and MP is larger than the random errors, and one of these sites must have a systematic timing error given that they differ by only 100 m in cross-track offset. In the geometry figure, time moves from right to left. In the nearly duplicated CW/MP chord pair, the MP points appear to the left of CW for both ingress and egress. The CW chord was obtained with a system similar in design to the heavily tested QHY174 systems and should be good to 1 ms or better. The 50 ms timing

uncertainty for the MP chord is consistent with the difference seen between the CW and MP chords. Note that the timing for MP in Table 16 shows only the random errors on the timing but does not include the 50 ms systematic error component. For the purposes of our analysis the MP data were excluded from the limb fitting rather than just deweighting the measurement. The ingress points for DK and Y07 indicate a local slope in that region that is consistent with the slope indicated by the next ingress points to the north and south. The uncertainties on the

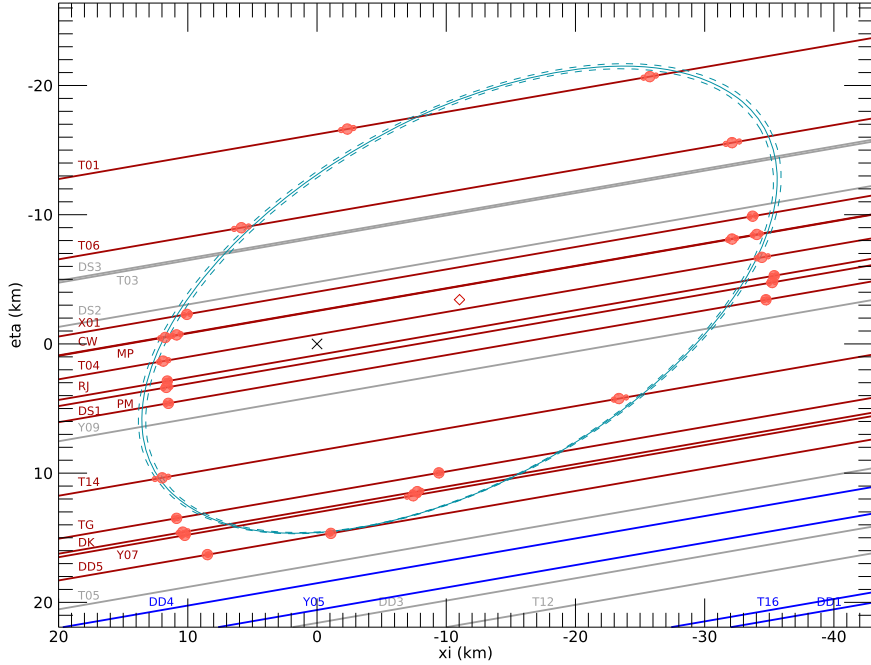


Figure 21. Limb profile for LE20191229. Shadow plane projection of occultation timing. These are tangent plane positions oriented as if looking down on the projected shadow as it would appear on the surface of Earth (see Appendix A for details). Orange circles are the measurements from Table 16; their individual (ξ, η) values are available in a machine-readable format (Table 17). The 1σ uncertainties, when visible, appear as half-size circles. The labeled lines show the track of the star across the object as seen at each site. Orange lines correspond to sites with positive detections, blue lines correspond to sites with negative constraints, and gray lines indicate sites unable to collect useful data. The cross indicates the predicted center based on the final orbit estimate. The diamond symbol indicates the center of the fitted ellipse.

Table 16
Occultation Timings for LE20191229

Team ID	UT Disappearance	UT Reappearance	Length (km)	Offset (km)
T01	03:33:39.233 ± 0.020	03:33:40.214 ± 0.019	23.8 ± 0.7	23.1
T06	03:33:39.137 ± 0.022	03:33:40.729 ± 0.023	38.6 ± 0.8	17.0
X01	03:33:35.950 ± 0.011	03:33:37.787 ± 0.011	44.5 ± 0.4	11.1
CW	03:33:38.716 ± 0.014	03:33:40.596 ± 0.014	45.5 ± 0.5	9.7
MP	03:33:26.145 ± 0.015	03:33:27.987 ± 0.015	44.6 ± 0.5	9.6
T04	03:33:39.677 ± 0.019	03:33:41.584 ± 0.015	46.2 ± 0.6	7.8
RJ	03:33:30.658 ± 0.006	03:33:32.628 ± 0.005	47.6 ± 0.2	6.3
PM	03:33:39.585 ± 0.009	03:33:41.548 ± 0.011	47.6 ± 0.3	5.8
DS1	03:33:39.032 ± 0.006	03:33:40.971 ± 0.006	47.0 ± 0.2	4.6
T14	03:33:39.902 ± 0.020	03:33:41.388 ± 0.021	36.0 ± 0.7	-1.0
TG	03:33:41.100 ± 0.005	03:33:41.952 ± 0.005	20.7 ± 0.2	-4.3
DK	03:33:40.335 ± 0.014	03:33:41.093 ± 0.015	18.4 ± 0.5	-5.5
Y07	03:33:35.153 ± 0.017	03:33:35.909 ± 0.011	18.4 ± 0.5	-5.7
DD5	03:33:41.883 ± 0.003	03:33:42.280 ± 0.002	9.8 ± 0.1	-7.5

Note. All times are on 2019 December 29. Offset is the distance perpendicular to the centerline of the last pre-event prediction.

timing are typically below 1 km, and seeing consistency between the sites at or below this level is an indication that the uncertainties are reasonable.

9. Shape

The full three-dimensional shape of Leucus is clearly much more complicated than a triaxial ellipsoid. These data should ultimately be combined with light curves from many apparitions to get a shape, but such an effort is beyond the scope of this work. There is, however, a rough correspondence between the limb profiles and ellipse as has been shown in the geometry figures. As a guide to interpretation of our results, the fitted ellipse values for the projected shape of Leucus are given in

Table 17. For each event we tabulate the number of chords obtained (Column (2)), semimajor axis (a), semiminor axis (b), and position angle of the minor axis. The position angle is measured eastward from north but is constrained to be between -90 and 90 until the actual spin pole is determined. Columns (6) and (7) are derived from the fitted ellipse properties: the projected area and the minor-to-major-axis ratio. The values that appear in parentheses for each column are the fitted ellipse properties for the smallest and largest ellipses, respectively, that are plotted on the geometry figures.

As imperfect as this treatment might be, there are clear trends to be seen in the profiles. We expected the semiminor axis to be constant if the spin pole is nearly normal to the line of sight given the light-curve results of Buie et al. (2018). The more

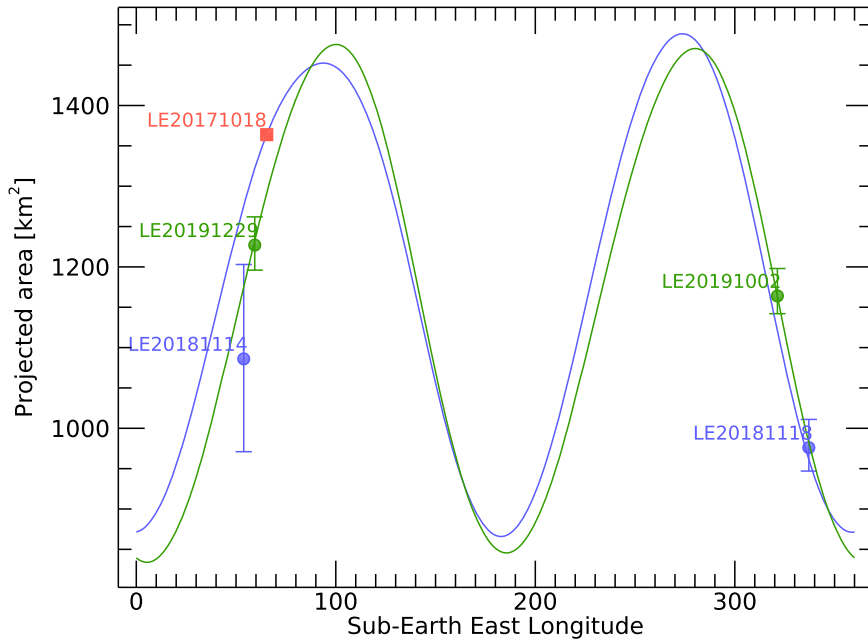


Figure 22. Shape constraints. The filled points indicate the cross-sectional area derived from the fitted ellipses for each event. The error ranges shown are not true uncertainties but are the area ranges from the ellipse limits. The solid curves show the light-curve constraint from 2018 (blue) and 2019 (green). The light curves are converted to area using a geometric albedo of 0.0367.

Table 17
Ellipse Fits to Leucus Occultation Profiles

Event (1)	Chords (2)	<i>a</i> (km) (3)	<i>b</i> (km) (4)	PA (deg) (5)	Area (km ²) (6)	<i>b/a</i> (7)
LE20171018	2	29.3 (fixed)	14.8 (fixed)	65.7 (72.0, 68.1)	1362 (fixed)	0.51 (fixed)
LE20181114	6	24.7 (22.9, 26.6)	14.0 (13.5, 14.4)	68.6 (65.5, 71.1)	1086 (971, 1203)	0.57 (0.59, 0.54)
LE20181118	9	20.3 (19.7, 20.9)	15.3 (15.3, 15.4)	69.2 (66.8, 71.1)	976 (947, 1011)	0.76 (0.78, 0.74)
LE20191002	4	23.9 (23.3, 24.6)	15.5 (15.6, 15.5)	61.9 (62.5, 61.4)	1164 (1142, 1198)	0.65 (0.67, 0.63)
LE20191229	14	27.5 (27.0, 28.1)	14.2 (14.1, 14.3)	59.9 (59.3, 60.8)	1227 (1196, 1262)	0.52 (0.52, 0.51)

Note. Values in parentheses give the values for the smallest and largest ellipses, respectively, for the ellipses shown in the geometry plots for each event. The LE20171018 fit was constrained as described in Section 2. The sky-plane values used to constrain the ellipse fits, corresponding to the orange data points in Figures 3, 7, 11, 14, 17, and 21, are available in a machine-readable format.

(This table is available in its entirety in machine-readable form.)

recent results from Mottola et al. (2020) are also consistent with this guiding expectation. The variation seen in our occultation results appears to be driven by the inherent inaccuracies in approximating the shape of Leucus with an ellipse and not by variations caused by a tilt in the rotation pole with respect to the line of sight. LE20181114 and LE20181118 are separated by just 4 days and 77° of rotation, and the viewing geometry did not change enough to significantly change the sub-Earth latitude or solar phase angle. This difference of 1.3 km in the minor axis is most likely related to the relatively poor approximation of the profile of Leucus by a perfect ellipse constrained only by our discrete chords. If so, the various measures of *b* are consistent with no variation and thus consistent with the prior light-curve work. We therefore adopt the average value of *b* = 14.8 km from Table 17 as the semiminor axis of the equivalent ellipsoid. Adopting this value is also equivalent to the condition that the rotation pole is strictly normal to the line of sight, and this condition is used for the subsequent analyses. Subsequent to this work, a formal pole solution based on light curves was provided by Mottola et al. (2020), where the presumption of a low obliquity is confirmed.

We leave the task of reconciling the occultation data, light curve, data, and three-dimensional shape models for future work. For this work, we will confine ourselves to constraints based on our simplifying assumptions. To address the other two axes of the ellipsoid, we must include constraints imposed by the light-curve data.

The properties of the fitted ellipses can be used to compute a cross-sectional area, which we find is a helpful quantity in checking and ultimately understanding our results. Figure 22 shows the cross-sectional area in comparison to the measured light curves from 2018 and 2019 (Mottola et al. 2020). The occultation measurements are the same data as found in Table 17, and the error bars represent the range of error implied by the ellipse limits derived for each event, rather than formal uncertainties. The solid curves show the Fourier series fit to the light curves from 2018 (blue) and 2019 (green) after converting from $H_V(1, 0)$ to projected area using the geometric albedo from Table 18. We compared the projected area based on the light curve to the area of the fitted ellipses from the occultation data. The plotted points are color-coded to help facilitate comparison to the correct year. Three of the four events from

Table 18
Geometric Albedo for Leucus

Event	Lon	$H_V(1, 0)$	p_V
LE20181114	53.85	10.727 ± 0.007	0.043 ± 0.005
LE20181118	337.10	11.035 ± 0.007	0.038 ± 0.001
LE20191002	321.35	10.828 ± 0.032	0.035 ± 0.001
LE20191229	59.37	10.765 ± 0.032	0.040 ± 0.001
Average	0.037 ± 0.001

2018 and 2019 match the Fourier series fit within the ellipse area range plotted. The LE20181114 occultation-derived area is somewhat low compared to the light curve, but this also happens to be from the data with the lowest S/N from the occultation. We cannot address the discrepancy given available data but consider it reasonable that the occultation area derived from this event is just lower than it should be owing to the poorer-quality data. The apparent agreement for the 2017 data is good to see, but the limited data from 2017 limit the usefulness of that agreement. At the accuracy level of analysis applied here, these measurements show an overall good agreement with light-curve photometry.

Table 18 contains the constraint on the geometric albedo of Leucus from the combination of the cross-sectional area provided in Table 17 and the absolute photometry from Mottola et al. (2020). To facilitate our analysis, the light curves from 2018 and 2019 are represented by fourth-order Fourier series fits to the photometry as a function of sub-Earth longitude for each year. Using this fit, we can compute an estimated absolute magnitude at any sub-Earth longitude. Note that the listed uncertainties are carried over from the light-curve mean and do not include any uncertainty in our knowledge of the longitude or discrepancy between the Fourier fit and the real light curve. Thus, for each event we combined the interpolated absolute magnitude and the projected area from the occultation and computed a geometric albedo. The weighted mean of all of the geometric albedo determinations is $p_V = 0.037 \pm 0.001$, which is very low, effectively at the limit for natural surfaces.

The projected area as a function of longitude shown in Figure 22 provides a means to constrain the three-dimensional shape of Leucus. As noted before, we take the semiminor axis of the ellipsoid (c') to be 14.8 km. The semimajor axis (a') can then be derived from the maximum area. Taking the average of the peak values from each light-curve epoch gives an area of 1482 km^2 and thus $a' = 31.9 \text{ km}$. The intermediate axis b' can be derived from the minimum area. Again, taking the average gives an area of 850 km^2 and thus $b' = 18.3 \text{ km}$. It is reassuring that the intermediate axis thus derived falls between the other two bounding values. Our final estimate of the ellipsoidal approximation to the shape of Leucus is thus $(a', b', c') = (31.9, 18.3, 14.8) \text{ km}$. Alternatively, the major axes give a shape of $63.8 \times 36.6 \times 29.6 \text{ km}$ and are definitely largely prolate. This result corresponds to an equivalent spherical diameter of 41 km. The prior results discussed in the introduction were $D = 42 \text{ km}$ from IRAS (Tedesco et al. 2002) and $D = 34 \text{ km}$ from WISE (Grav et al. 2012). Our result is in very good agreement with the IRAS result but not with WISE. We looked at the WISE observations and found that they were taken over a limited range of time and do not represent an average over the entire light curve, accounting for its lower size estimate. The uncertainty on our shape result is dominated by the effects of topography, not the formal

measurement uncertainties in our data. For a more detailed analysis of the shape, see Mottola et al. (2020).

Having this size provides important contextual information from which to understand the topography, where we use this term to describe any deviation from an ellipsoidal shape. The LE20181114 event shows positive and negative relief on the order of 2–3 km. The minimum horizontal distance limits from peak to trough are of the order of 10 km. The improved chord density for LE20181118 shows topographic structures, some of which correlate across two or more chords. At this aspect there is a large concavity that is 30 km across and 4 km deep. Furthermore, there appears to be a topographic high on both sides of this concavity. It is always a risky proposition to provide geologic interpretations based on occultation data, but this feature is certainly consistent with a large impact structure. There are two other smaller concavities, one 14 km across and 2 km deep and the other 12 km across and 1–2 km deep. The dimensions of these structures are all limited by how close the actual feature is to being exactly on the limb. We cannot distinguish between a shallow feature on the limb and a deep feature that is rotated off the limb. The shape from LE20191002 once again shows a very large topographic structure on the southern end of Leucus and is consistent with the 30 km wide concavity seen in the LE20181118 data. Note that the sub-Earth longitude for these two events is very similar, with just 16° of rotation between the two.

Our best limb profile comes from the LE20191229 event. There are clear topographic signatures in these data as well, and the geometry is much closer to that for the LE20181114 event. On the southern end of Leucus, there are once again raised areas of 2 km in roughly similar locations to what was seen in LE20181118 data, but there is no obvious concavity of a similar shape or depth. This feature on the southern end could be tilted toward us at a sub-Earth longitude of 340° and thus suppressed somewhat when viewed from 60° .

Making full sense of Leucus will clearly require more data. Some improvement can be had with continued Earth-based observations, but the Lucy encounter can certainly provide essential geologic context to the features seen in the occultation data.

The shape for Leucus we derive here implies a much longer central chord than what was observed at the one station for LE20171018 (see Figure 3). That chord length was 19 km, and yet it was slightly closer to maximum light (peak brightness) compared to LE20191229 as shown in Figure 22. The estimated projected area for the 2017 event is 1364 km^2 based on the 2018 light-curve fit. That area predicts a semimajor axis of the projected ellipse of 29.3 km. Thus, a central chord could have been as long as 58.6 km, though it would have likely been a little shorter than this for the axis not being perfectly aligned with the direction of motion of the shadow. Assuming perfect alignment of a perfect elliptical profile, chord S01 was actually a grazing chord that was 14 km from the centerline and likely was responsible for both of the 2018 occultations occurring south of the predicted centerline.

Given an occultation at maximum light, a central chord at maximum light would be close to 64 km. For future occultation events, getting a better determination of the shape and pole can enable us to provide enough coverage at maximum light if the major axis is significantly tilted with respect to the down-track direction.

Table 19
Leucus Occultation Astrometry

Site ID	UTC	Latitude (deg)	E Longitude (deg)	Altitude (m)	R.A.	Decl.	Δ (au)
S01	2017/10/18 00:01:11.289	+40.086778	-88.196194	224	18:41:41.85152	-15:54:20.5539	5.604
T11	2018/11/14 03:07:47.310	+32.942445	-111.096097	881	20:40:51.61371	-07:13:22.2179	5.356
T16	2018/11/18 02:42:14.603	+29.449299	-100.951760	354	20:42:49.06726	-07:11:42.4799	5.415
A04	2019/10/02 07:15:54.822	+41.529037	-120.177122	1434	22:41:10.11000	+06:45:38.7034	4.210
T04	2019/12/29 03:33:40.648	+33.833056	-111.906110	762	22:53:00.12714	-04:20:35.6333	5.337

Note. R.A. and decl. are given in EME2000 coordinates and are topocentric measurements. All topocentric locations are referenced to the WGS84 datum. The last column is the geocentric distance at the given time.

10. Astrometry

Given that we have such high precision on the star locations, occultations provide a means to extract similarly high precision astrometry from the event itself. The limb profiles from an occultation contain such position information, and it is straightforward to convert to astrometry. The key measurement is the location of the body center. If the body has a simple shape, this can be done extremely well. In fact, the position of the center of the body relative to the star is often better determined than even the high-precision Gaia DR2 positions. With the distinctly distorted profile of Leucus, the body center and, by assumption, the center of mass are not as easy to locate. Until a full three-dimensional model can be generated, we can only estimate the errors on finding the body center.

Table 19 lists the astrometry derived from the Leucus occultations presented in earlier sections. We do not list formal uncertainties, but all reported digits are considered to be significant. The position of the body center appears to be good to roughly 1–2 km, even considering the effects of topography. For reference, at a distance of 4 au (distance at opposition), the scale on the plane of the sky when Leucus is observable ranges from 2800 to 4000 km arcsec⁻¹ over its 12 yr orbital period. A 1 km offset would map to 250–360 μ as, which is comparable to the uncertainties on the Gaia DR2 positions. Better results may be possible by combining a detailed 3D shape model with improved Gaia positions with later catalogs, but such an improvement is well beyond the scope of this work. Note that in our own fitting we currently adopt a uniform 5 km uncertainty for the occultation positions when used to constrain the orbit. These uncertainties can and will evolve as we learn more about the shape of Leucus.

11. Conclusions

The occultations of Leucus presented here provide an important data set from which to constrain a model of its shape. The longitude coverage for the four multichord events could be more evenly distributed, but that is difficult to control with occultation observations. Nonetheless, if we have to pick and choose which occultations to pursue in the future, the longitude sampled will clearly be an important consideration. These data will become even more useful as the body of light-curve photometry grows and we fill out our coverage from the full range of viewing geometries over the course of its 12 yr orbit. By combining the photometric and occultation data, we can improve on the three-dimensional shape of Leucus and its spin pole (see Durech et al. 2011; Satō et al. 2014; Hanuš et al. 2017). Thanks to the occultation data, we will also be able to

retrieve more than just a convex-hull shape model (Mottola et al. 2020).

The light-curve data already indicated a highly nonspherical shape. Our occultation data take this one step further and show a very irregularly shaped body that is somewhat superficially described by an ellipsoid. Relative to the ellipsoidal shape, there is correlated topography over 10–30 km that is a significant fraction of the size of the object. It is clear that Leucus does not have a relaxed shape, and the most ready explanation is severe surface modification from cratering or other similar high-energy deformation processes. Such highly modified surfaces are not uncommon in the solar system, though perhaps most of the more common nonspherical objects that we know are much smaller. However, the second-largest main-belt asteroid, Vesta, has large cratering features, so it is clear that size alone does not protect against survival of a collisionally evolved surface (Marchi et al. 2012). In the case of Vesta, there is an entire family of objects that are believed to be ejecta from some past impact (Marchi et al. 2015). These are known as much through their common and easily identifiable spectral signature as they are for their orbital properties. Perhaps there could be a similar family of ejected material from Leucus, though no such associations are known at this time. Leucus is an order of magnitude smaller than Vesta, so it might be reasonable to expect that the ejecta from Leucus would also be smaller by a similar factor. Given that Leucus is at 5 au, detecting and characterizing such material would be much harder because the fragments would be both smaller and much farther away than the Vesta family.

The occultation astrometry has already provided considerable improvement to the orbit estimate for Leucus. As the two 2019 events showed, we can now predict an occultation with an uncertainty much smaller than the size of the object. Additionally, the post-fit residuals for the occultation astrometry are similarly much smaller than the size of the object. The small residuals for these five independent constraints indicate that there is no large unseen mass orbiting Leucus. Assuming uniform densities and albedo, as well as a circular orbit of a given semimajor axis, an upper limit to the size and mass of a secondary can be computed for a given limiting barycentric wobble. Using our adopted 5 km uncertainty of the astrometry as the upper limit to the wobble, a secondary must be no larger than $D = 12$ km for $a = 10 * r_1$, where a is the semimajor axis and r_1 is the spherical effective radius of Leucus, $r_1 = 20.5$ km. For a range of a/r_1 from 60 down to 5, the secondary diameter limit ranges from 7 to 15 km. The corresponding brightness ratio of the secondary to the mean for Leucus ranges from 0.025 to 0.14. Adding the lack of detection of any additional objects either with occultations or with

searches by the Hubble Space Telescope (Noll et al. 2018), the likelihood of a large satellite is very low. Smaller satellites cannot be completely ruled out, but we leave more rigorous quantitative estimates of this limit to future work.

The surface of Leucus is clearly very dark with $p_V = 0.037$. The surface is also somewhat red with $(V - R) = 0.466$. This is a typical color for Jupiter Trojans, as well as a typical albedo (Fornasier et al. 2007; DeMeo et al. 2015; Emery et al. 2015). The color is not as extreme as what is seen in the TNO population (Belskaya et al. 2015). Comparing Leucus to Arrokoth brings out far more differences than similarities. Leucus is darker, is less red, and has a highly modified surface compared to Arrokoth. The data to be provided by the Lucy flyby will be a crucial data set to constrain properties of the Jupiter Trojan population that lies at a midpoint between the highly modified main-belt asteroid population and the far more pristine cold classical Kuiper Belt objects.

This work was largely supported by the Lucy Mission, which is funded through the NASA Discovery program on contract No. NNM16AA08C. Funding for RECON was provided by grants from NSF AST-1413287, AST-1413072, AST-1848621, and AST-1212159. Funding for F. Marchis was provided by a grant from NSF AST-1743015. Pan-STARRS is supported by the National Aeronautics and Space Administration under grant No. 80NSSC18K0971 issued through the SSO Near Earth Object Observations Program.

The Pan-STARRS1 Surveys (PS1) and the PS1 public science archive have been made possible through contributions by the Institute for Astronomy, the University of Hawaii, the Pan-STARRS Project Office, the Max-Planck Society and its participating institutes, the Max Planck Institute for Astronomy, Heidelberg, and the Max Planck Institute for Extraterrestrial Physics, Garching, Johns Hopkins University, Durham University, the University of Edinburgh, the Queen's University Belfast, the Harvard-Smithsonian Center for Astrophysics, the Las Cumbres Observatory Global Telescope Network Incorporated, the National Central University of Taiwan, the Space Telescope Science Institute, the National Aeronautics and Space Administration under grant No. NNX08AR22G issued through the Planetary Science Division of the NASA Science Mission Directorate, the National Science Foundation grant No. AST-1238877, the University of Maryland, Eotvos Lorand University (ELTE), the Los Alamos National Laboratory, and the Gordon and Betty Moore Foundation.

Thanks to all our other essential contributors for the observing campaigns: Scott Adams, Seth Anthony, Teri Ast, David Barrows, Becky Bobick, Dick Bobick, Bill Boynton, Jesus Bustos, Brian E. Cain, Rene Cardenas, Catalina Chapman, Nina Chevalier, John G. Compton, Dorey W. Conway, Kenneth B. Conway, Richard L. Cunningham, Chris Erickson, Robert Ewing, Paul S. Facuna, Rick E. Frankenberger, Corbin Fredland, Phylis L. Hanna, Hugh C. Harris, Ryuga Hatano, Kevin R. Healy, Frances Healy, Jonathan Jacob Hernandez, Mark Hickinbotham, Tyler Frederick Hilgendorf, Bekah Hillard, Kimberly Jeanine Hollingsworth, Sam F. Insana, Robert A. Jones, Richard L. Karohl, Jim Kochenderfer, Christopher Koers, Kevin R. Kotara, Svitlana Kroll, Arnaud Malvache, Laurent Marfisi, Alexis Martin, Keitha McCandless, Mel E. McClure, Randy McKnight, Chuck McPartlin, Randle L. Mellen, Terry R. Miller, Crystal Moczygemba, Rod G.

Moorehead, Sean Moss, Juan Munoz, Olivia Newton, Nidhi R Patel, Anthony J. Pistilli, Ryan Rickerson, Matthew Riehle, Susan K. Rost, Jack Rost, Eric Sahr, Jade Salazar, Ramsey Schar, Jim Scotti, Tiffany Severson, Myron Smith, Maria Stothoff, Stuart A. Stothoff, Emma Tibay, Kimberly Valenzuela, Kathryn Volk, Dannie Wayne Wagoner, Michelle Wilkinson, William Wilkinson, Robert P. Williams, Peggy Yeargain, Michael K. Young, and Amanda M. Zangari.

Appendix A Coordinate System for Limb Profiles

The limb geometry plots presented in this work and Buie et al. (2020) are based on a rigorous mathematical framework to facilitate the extraction of astrometry from any well-observed occultation event. It is not quite the same as other coordinate systems in common use for analyzing occultations, and so we provide a complete description here. Note that this method is meant for use with small bodies that also have no atmospheric signatures in their occultation light curves. Development of this method was driven by available tools and the desire for simplicity. Converting those coordinates and the resulting plot to something that “looks right” is another matter entirely.

The first step is to describe the coordinates. We use a tangent plane on the celestial sphere, and by choice this is tied to J2000 (EME2000) coordinates. The tangent point that defines this plane is the apparent position of the occultation star for the epoch of the occultation. The epoch used is the date and time of geocentric closest approach between the object and the star. Since the star position does not change very fast, we do not worry about a more rigorous choice of time. The star position is corrected for proper motion and parallax.

The tangent plane coordinates are (ξ, η) , and we use the conventions and derivations found in Green’s “Spherical Astronomy,” Section 13.2, starting on page 310 (Green 1985). Figure 23 shows the geometric definition of (ξ, η) as provided in Green. Green refers to (ξ, η) as the “standard coordinates,” but this term is not always recognized. We will refer to (ξ, η) as the tangent plane coordinates. From Figure 23 we see that η is in the same direction as decl. (D) and ξ runs in the same direction as R.A. (A). Also notated on the plot is the reference point for R.A. (Υ), the center of the celestial sphere (C), the celestial pole (P), the star location (T), and the tangent point defined by the star celestial coordinates $X = (\alpha, \delta)$.

Equation (13.12) is the relevant transformation equation from Green and is reproduced here:

$$\begin{aligned} \xi &= \frac{\cos \delta \sin(\alpha - A)}{\sin D \sin \delta + \cos D \cos \delta \cos(\alpha - A)} \\ \eta &= \frac{\cos D \sin \delta - \sin D \cos \delta \cos(\alpha - A)}{\sin D \sin \delta + \cos D \cos \delta \cos(\alpha - A)}. \end{aligned} \quad (A1)$$

The IDL program `astrd2sn.pro` computes this transformation, with the resulting tangent plane coordinates given in either radians or arcseconds. The routine `astsn2rd.pro` provides the reverse transformation. These routines use a manipulated form of the transformation equations to facilitate the computation. There are three things to note here: (1) (ξ, η) are rectilinear coordinates, unlike (A, D) ; (2) as used in this work, the “units” on (ξ, η) are arcseconds; (3) there is a singularity in the equations, and the tangent point cannot be evaluated exactly at

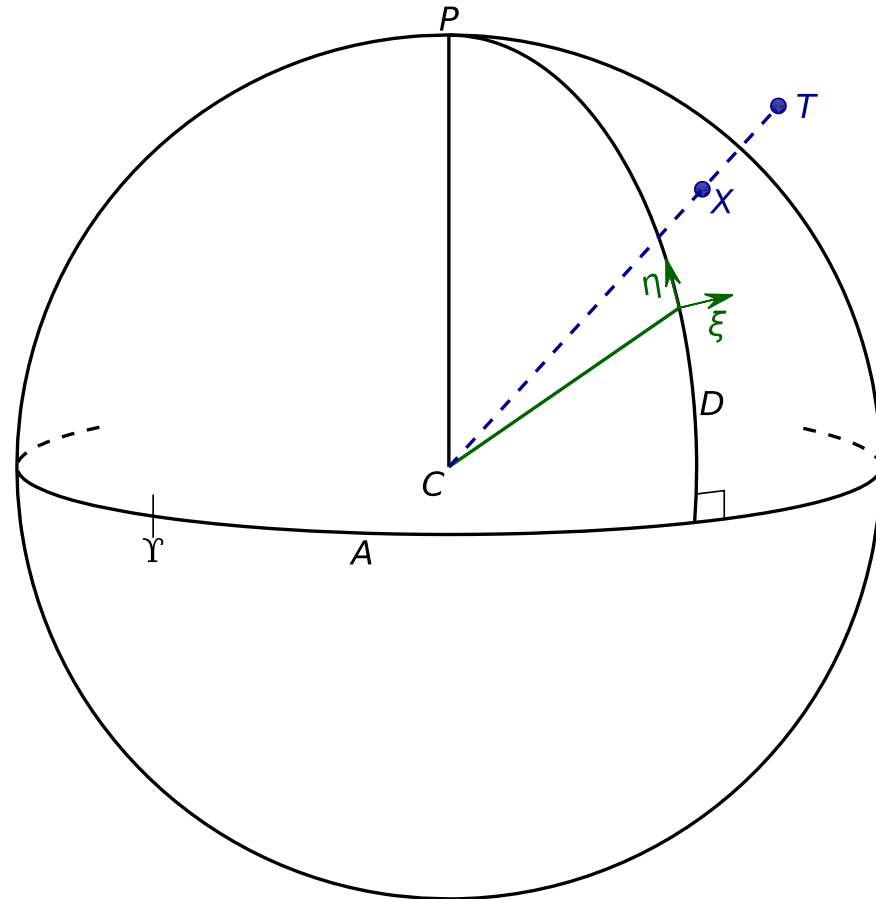


Figure 23. Tangent plane coordinates (ξ, η) . The star, T , projects to the celestial sphere at $X(\alpha, \delta)$ defining the plane. The tangent plane coordinates are relative to the tangent plane at (A, D) . R.A. (A and α) are measured from the reference point, Y . See text for more details.

the pole. The origin of the tangent plane coordinates is, of course, the position of the star.

For a given observer, there is a unique transformation between the object and the star in the tangent plane that depends on the time and the position of the object at that time. By specifying the observer, you must know the position of the observer at the specified time, usually a latitude, longitude, and altitude. An occultation data set consists of a set of measurements taken at specific times. Thus, you can compute the (ξ, η) coordinates of the center of mass of the object at the given time for the given observer. In the case of the disappearance or reappearance of the star, the time is usually somewhere during a single integration, and the derived time for a given observer uniquely identifies a point in the tangent plane.

This description is exactly the coordinate system used in the limb plot diagrams in this work. The lines drawn on the plot show the path of the center of the body relative to the star as seen by each observer. The limb points plotted give the position of the center of the body at the time of specific events. The plots generated do indeed give you the outline of the object in this coordinate system. Relating this outline to what you would “see” is quite another thing.

Relating these limb profiles to what you would “see” requires defining what you mean by “see.” There are two conventions to discuss (though there could be more). The first (let us call this View 1) is to imagine what the object looks like on the plane of the sky as if you had as much magnification as

you wanted. You can choose to orient your view with celestial north up and celestial east to the left, and the object would be presented at some orientation. The second option (View 2) is to imagine looking down on the shadow cast on Earth (not including any projection effects onto a sphere). The exact details of where you are looking from do not really matter; you just want to see how the moving shadow on the surface of Earth relates to the combined experiences of the observers. Each of these views has its own merit and is useful.

At this point it comes down to how to relate the tangent plane coordinates to the view. The transformation from a (ξ, η) limb profile to View 1 can be thought of in the same way that a pinhole camera works. The desired image should be upside down and backward, basically a transpose of each axis. Going from View 1 to View 2 involves a left–right reversal. The plots in this work adhere to View 2. A potentially confusing factor is that (ξ, η) is a left-handed coordinate system and requires an additional x -axis reversal to match the coordinates to the view.

Appendix B Support Astrometry and Orbit Fitting

The support astrometry for this project evolved over the course of this project from “traditional” methods essentially unchanged over the past few decades to include important new elements to reach a higher level of precision than previously possible. For the purposes of this discussion, the astrometry data fall into four distinct groups: historical data from the MPC, observations obtained by the Panoramic Survey Telescope and

Rapid Response System (Pan-STARRS), observations from Gaia DR2, and observations from the SwRI robotic telescopes sited at Sierra Remote Observatories (SRO), 50 km northeast of Fresno, CA. The historical data are a very heterogenous group and in particular are measured with respect to a variety of astrometric reference catalogs, and that information would still be difficult to obtain even if an easy correction to a better catalog were possible. All of the other data sets we used are either from or referenced to the Gaia DR2 catalog.

The MPC data we used are those generally available to the community and are limited to the information that is encoded in the long-standing 80-column format. This format has some important limitations. The precision of the published positions is limited to ~ 10 mas owing to the number of significant digits supported by the data format. Also, almost no supporting data about the observations are published in this form. Only the observatory site code is given for the data. The most important limitations are the lack of measured or estimated uncertainties on the positions, and there is no information available about the astrometric support catalog used. As a result, these data have the largest contributions of both systematic and random errors. We tried using an approach similar to Vereš et al. (2017) to estimate the random errors and systematic errors of the astrometry on a site-by-site basis. An alternate and far simpler approach was to set the uncertainty for all MPC data to 600 mas. We chose the latter approach for its simplicity and because the other approach did not give us a better fit. The choice of 600 mas was guided by looking at the residuals by data set. When the MPC data were overweighted, other smaller yet higher-precision data sets started showing unrealistic residuals, which we describe as “tension” between data sets. We thus chose the smallest value that eliminated this tension. The chosen value was not rigorous but was picked as a reasonable choice. Though lower in accepted precision, this data set provides the longest baseline of astrometric constraint.

The data from Gaia DR2 are the most straightforward to incorporate. The observations come with a detailed characterization of both random and systematic error components. These uncertainties are all characterized by a highly elliptical Gaussian envelope, where the minor axis of the ellipse is nearly a factor of 100 smaller than the major axis. We use all of the Gaia data as is without any scaling of the uncertainties or using any subsets of the data. These data provide the strongest positional constraints of all four data sets but have a limited time range and are not particularly close to the epoch of the occultations.

The data from Pan-STARRS span 2009–2019 and largely come from the archive over the lifetime of the survey (Chambers et al. 2016) but also including new observations. Coauthor Weryk has tools that facilitate the easy extraction of astrometry of any known object that is brighter than roughly $V = 22.5$, providing excellent data on all of the Lucy targets. There are already some data in the MPC archive for Pan-STARRS. We take care to remove those data from the MPC largely owing to the older data being measured with a pre-Gaia DR2 catalog. However, the data we use bypass the limitations imposed by the MPC data format. We get full precision positions with point-by-point uncertainties, and all data are known to be reduced against the Gaia DR2 catalog. These data provide roughly 9 yr of data, covering a significant fraction of a single orbit around the Sun for the Trojans. This data set is rather sparse but is very well behaved within the provided

uncertainties and is nicely complementary with the higher-precision but shorter-arc Gaia data. Given the quality of these data, we usually truncate the MPC data and do not take any from 2010 and later. The Pan-STARRS data cover this later time frame and are much better understood and of higher precision.

Gaia plus Pan-STARRS data alone give a better occultation prediction than is possible with the MPC data by themselves. The orbit based on just the MPC data is good enough for searching for candidate occultation events but not at all adequate for a practical occultation deployment for objects the size of Leucus and Orus. The Gaia plus Pan-STARRS orbit solution is much improved but was limited by not having data close to the time of the occultations. The near-term data were provided by the data from the SwRI robotic telescopes.

The SwRI facilities consist of two PlaneWave CDK-24 telescopes on the Software Bisque Taurus equatorial fork mount. The first system brought online was the David C. Slater telescope, which was installed in 2017 December. The second system is the William C. Gibson telescope, which was installed in 2019 July. Both telescopes are located at the Sierra Remote Observatories (SRO) facility (MPC code G80), and both currently use an Andor Zyla sCMOS camera. The telescopes are used at the RC focus with an $f/6.5$ beam and nominal scale of $52''.2\text{ mm}^{-1}$ image scale. The camera detectors have 2560 by 2160 pixels, where the pixel size is $6.5\text{ }\mu\text{m}$. The gain of the camera, set and measured at the factory, is 0.45 e-DN^{-1} , and the read noise is nominally 1.3 e-. We do not use a mechanical shutter, and the full-frame readout time is less than 1 ms with the rolling-shutter mode we use. Due to the hot-pixel behavior of the camera, exposure times are limited to no more than 30 s. Both telescopes have identical sets of filters: B , V , g' , r' , i' , 8900 \AA (CH_4), and an ultrawide $V+R$ interference filter (referred to as the VR filter). Typical seeing for this site is $1''\text{--}2''$, and with our image scale the PSF is oversampled. All of our data for this project were taken with the VR filter.

These two telescopes are operated as robotic facilities with real-time scheduling of observations. So far, we restrict a given target to just one of the two telescopes on a given night. The processing is identical for both systems, and the identity of the telescope used does not matter for the final astrometry. The pipeline processing of the data includes the usual steps of building supercalibration frames and applying bias, dark, and flat fields to the images. There is a pixel-processing step that removes the residual hot pixels from the data. At the very end, automated astrometric solutions are generated for each data frame based on the Gaia DR2 reference catalog. This astrometric solution is a simple linear fit. There are no measurable higher-order terms.

Before measuring the object, the individual images are stacked in sets of 10 images. Two stacks are generated, one registered on the sky plane fixed with respect to the stars, and the other registered on the sky plane comoving with the object. This process is similar to long-standing techniques for combining images to avoid trailing losses on moving objects (see Cochran et al. 1995; Bernstein et al. 2004; Buie et al. 2012; Lauer et al. 2018). The average FWHM of the sources in the star-stacked image is measured, and this becomes the radius of the synthetic aperture for photometry and astrometry. The stacked images are then refitted for an astrometric solution. Given how the stacks are constructed, the same astrometric solution applies to both stacks, and then it becomes simple to

take the (x, y) position of the object and extract its apparent position on the sky.

In the course of our work to predict occultations for Lucy, we discovered systematic errors in our astrometry. Eventually, this was determined to be due to differential refraction. Basically, all sources in the image are subject to refraction by Earth's atmosphere. The total amount of refraction is quite large, but the mean amount is removed as a natural consequence of the astrometric solution derived for each image. An interesting discussion of this problem can be found in Stone (2002). The methods used by Stone to remove refraction effects do not work for our observation owing to the lack of supporting reference observations. As a result, we were forced to come up with a method that would work for the data we have. Our approach was to find a suitable and useful approximation that would work on a single image. The following discussion provides the details of the approach we developed.

The amount of refraction is computed with the Buie IDL library routine, `refrac.pro`. From its documentation, the calculation is based on a few different sources. The index of refraction of air at the base of the atmosphere can be calculated (see `airindex.pro`). This function is based on the formulae in Filippenko (1982) for the index of refraction of air. The conversion from relative humidity to vapor pressure is from the CRC Handbook (2007). Given the index of refraction, the bending is computed from the formula on p. 55 of the old Explanatory Supplement to the Nautical Almanac (Nautical Almanac Offices of the United Kingdom and the United States of America 1974). This formula has been modified by removing the h/ρ term. The explanatory supplement does not indicate that this is legitimate, but this computation was validated against a more empirical formalism from Eisele & Shannon (1975, NRL memo 3058). Eisele and Shannon do not indicate the wavelength of light used, but using $0.56 \mu\text{m}$ and comparing for the same input conditions (dry air only), the refraction computed agrees to within $1''$ down to 51° zenith angle and is good to $10''$ down to 80° . In principle, the amount of refraction depends on the wavelength of light, temperature of the atmosphere, absolute pressure, and relative humidity. In practice, it is sufficient to use mean values for the observatory for temperature, pressure, and humidity, as these components contribute less than 1 mas. The dominant component for the correction is the mean wavelength and of course the zenith distance.

Thus, the refraction for each source depends on its spectral energy distribution (SED). We make several approximations here to speed up the calculation. First, we compute the refraction relative to the mean wavelength of the comparison stars. Second, the SED is captured by computing the pivot wavelength. This pivot wavelength is the point within the bandpass that is the midpoint in the detected SED given by the combination of the SED of the source multiplied by the detected quantum efficiency (DQE) of the camera/filter/telescope system. The DQE is approximated by multiplying the filter transmission curve with the detector quantum efficiency. In principle, we should compute the mean wavelength of the actual sources used in the astrometric fit and then correct each star to this mean wavelength before performing the final fit. This level of sophistication has not yet been implemented in the processing pipeline. Instead, we had to implement a post-processing approximation. For this, we take the list of Gaia sources within the circular equivalent field of view for

our camera down to an average magnitude limit of $G = 18$. The pivot wavelength is computed for each of these sources, and the mean of this set is taken to be the mean wavelength for the solution. In the end, the differential refraction correction comes down to computing the shift for pivot wavelength of the object relative to the mean wavelength for the stars used for the solution. For the object colors we used $(V - R) = 0.466 \pm 0.025$ for Leucus and $(V - R) = 0.457 \pm 0.021$ for Orus. The color for Leucus comes from Mottola et al. (2020), and for Orus we used a preliminary determination provided by Mottola (private communication).

Figure 24 shows the amount of differential refraction computed for the Orus data set from SRO. The result for Leucus (not shown) is similar. The Orus data set contained 1558 observations covering more than a full apparition. Note that technically refraction is always away from the zenith, but the differential refraction is measured against the refraction for the mean star color in each image and so can be either positive or negative. Sources that are redder than the mean star color appear to shift toward the zenith, and sources that are bluer shift away from the zenith relative to the astrometric solution for the image. The plotted corrections are technically not correct since we used a sea-level atmospheric pressure. However, this mistake was not discovered prior to the OR20191104 deployment. The difference in correction for the solid black and red curves shows the proper altitude correction for the largest color difference between the stars and Orus. While this error is a bit of a nuisance, it leads to a systematic shift in the prediction smaller than the uncertainty on the size of Orus. The overall shift (regardless of altitude) was significant and larger than the size of the object. Figure 25 shows a breakdown of the refraction correction for this same data set. For our observatory and the range of zenith angles, the differential refraction correction was as large as -40 mas. At the time of observation, Orus was always somewhat low in the southern sky, and the refraction correction was always important unless the stars happened to be the same color as Orus.

In principle, this same correction should be applied to the Pan-STARRS data, but the magnitude of the shift is greatly reduced compared to our SRO data because of the higher elevation of the Pan-STARRS observing site and the smaller zenith angle due to the more southerly location. Given that our astrometric data set is dominated by the SRO data near the time of the events, the value in correcting the Pan-STARRS data was limited, and we chose to skip this step. Eventually, we hope to incorporate this correction even for Pan-STARRS, but until then we carry an estimated systematic error contribution into the final deployment plan for each occultation.

One lesson learned from the corrections applied to the Orus astrometry is that ignoring this effect can lead to very subtle systematic errors in the astrometry. The colors of the reference stars are not randomly distributed across the sky, and each observatory has a different magnitude owing to the observatory latitude, time of observation within a night, and site elevation. Even with these variations, the ensemble of all observations will still have a systematic quality that will vary on a timescale comparable to the synodic period. Orbits derived from uncorrected data will likely be more than adequate for most applications. However, high-precision work needed by occultation predictions, spacecraft navigation, and perhaps even mass

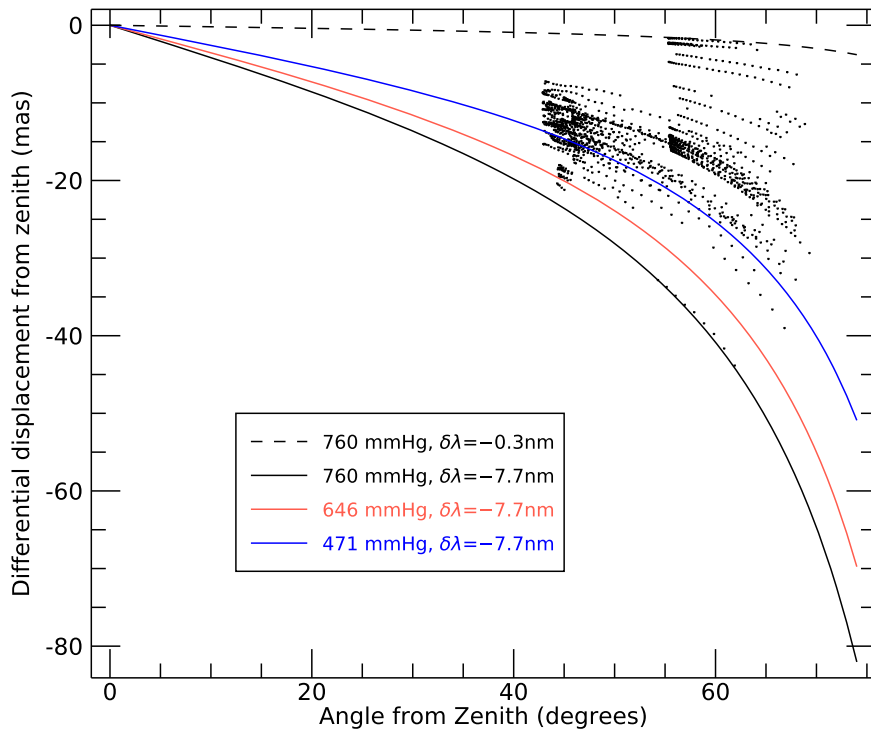


Figure 24. Differential refraction correction for Orus. Each dot on the graph represents one image, its zenith distance and the correction computed. The corrections were computed for atmospheric pressure of 760 mmHg, temperature of 0°C, and humidity of 0%. The solid black curves are plotted for these same conditions but for the largest wavelength difference (solid curve, -0.3 nm) and the smallest wavelength difference (dashed curve, -7.7 nm). The red curve is the refraction correction for a pressure of 646 mm Hg appropriate for 1400 m elevation at SRO. The blue curve is the refraction correction for a pressure of 471 mmHg appropriate for 4000 m elevation, similar to Manua Kea and Haleakala.

determinations from perturbations will need to consider this correction.

The final step in the process is clearly estimating the orbit of the target body. The methodology of this approach follows very closely on our prior work for Arrokoth (Porter et al. 2018; Buie et al. 2020). Simply put, we track all uncertainties of each measurement as a point cloud of measurements distributed according to their probability density function (pdf) on the sky plane at the time of measurement. Note that we do use iterative bad-point rejection, and most values found to be discrepant by 2σ or more are usually excluded, but this process is manually supervised. This supervision is most important for occultation data, which are never excluded regardless of the post-fit residuals. With our approach we can incorporate non-Gaussian errors, asymmetric uncertainties, or symmetric Gaussian uncertainties. For the Orus data, we used Gaussian covariances that were converted to discrete pdf's. The orbit estimate solves for a pdf of a Cartesian state vector that best matches the data. This pdf can then be sampled at some later time in any desired coordinate system to produce an expected value for the position and an associated probability distribution. For occultations it is quite useful to project this pdf into a frame of reference aligned with the down-track and cross-track directions of shadow motion across Earth. We can, if necessary, propagate non-Gaussian errors all the way from measurement to occultation prediction, but so far using a Gaussian approximation for the final pdf for an occultation works well enough and is much simpler to propagate to deployment support information such as ground-track maps that guide our teams to relevant observing locations.

Table 20 provides a focused summary of our prediction efforts for the two Orus occultations. A similar summary could

be provided for the Leucus predictions, but the case we show was the most influential for guiding our efforts throughout this entire project. Column (1) gives the date on which an orbit estimate was generated. We only show those estimates that were propagated forward to a ground-track prediction. Most of this work was directly focused on preparations for the OR20191104 event. Column (2) provides the cross-track offset of the predictions based on these orbits. To do this, we created a fictional observing location in Australia that is on the centerline of the 2019 October 28 prediction. Since OR20191104 was clouded out, we do not have ground-truth, but this gives us a fixed reference point to see the shifts produced by the different data sets used for the orbit fit. This offset is given in km, and a number approaching the size of the object is of great concern. In parentheses, this offset is also given in mas to make it easier to appreciate the scale of correction in the astrometry that will ultimately matter. Columns (3) and (4) give the cross-track offset of the observing sites from Table 9 for the OR20190907 event. Recall that S01 was a positive detection and S02 was a negative constraint, and their relative spacing was about 20 km. Column (5) gives the cross-track uncertainty for OR20190907 for that orbit, while Column (6) gives the same for OR20191104. All of the uncertainties are in the range of 2–4 km; thus, an offset as large as 20 km for S01 would indicate an orbit estimate that is likely inconsistent with that positive detection.

The right half of the table summarizes the amount of data used from each of our astrometric data sources. Column (7) gives the number of observations taken from the MPC data set. Many of these orbit solutions use no MPC data at all. The two shown with ~ 400 points were restricted to 2009 data and earlier. The full range of dates in the MPC data cover 1998

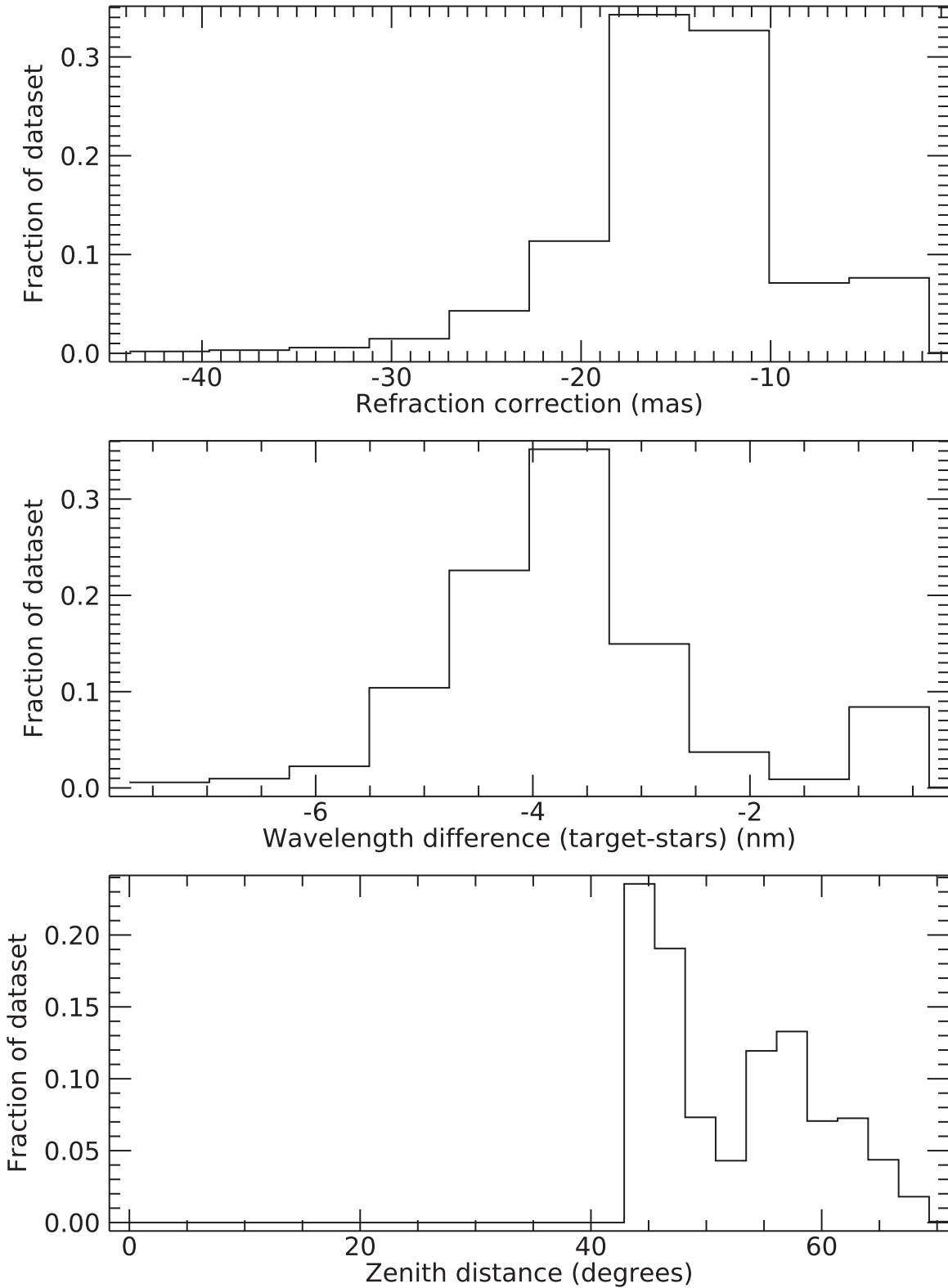


Figure 25. Distribution of Orus measurements from Figure 24. The mean refraction correction was -15 mas. The mean wavelength of Orus was 607.9 nm. The mean target minus star wavelength difference was -3.6 nm. The smallest zenith distance was 43° , and the mean zenith distance was 52° .

November 10–2019 May 21. Throughout this project it was very challenging to prevent the MPC data from adversely affecting the fit to other data sets, and it was usually easiest to just suppress those data. Column (8) lists the number of observations from the Pan-STARRS data. These data all span

2010 July 17 to 2018 August 13. This data set provides the longest arc for astrometry that is based on the Gaia DR2 catalog. The cases with significantly smaller amounts of data used were from an overly aggressive bad-point rejection filter. All of the orbit fits use all Gaia data at the published weight for

Table 20
Prediction Trends for 2019 Orus Occultations

Fit Date	xtrack km (mas)	S01 km	S02 km	σ_{0907} km	σ_{1104} km	MPC	PS2	Gaia	SRO	Occ	Total
(1)	(2)	(3)	(4)	(5)	(6)	(7)	(8)	(9)	(10)	(11)	(12)
2019-08-29	-5.5 (-1.5)	3.6	-17.7	2.7	2.6	0	71	81	469	0	621
2019-10-02	-38.7 (-10.7)	-22.3	-43.6	...	3.4	401	156	81	798	0	1436
2019-10-10	-35.6 (-9.9)	-20.4	-41.7	3.6	3.2	0	127	81	823	0	1031
2019-10-16	-36.0 (-10.0)	-20.8	-42.1	3.9	3.5	0	149	81	844	0	1074
2019-10-18a	-47.9 (-13.3)	-22.9	-44.2	4.2	5.6	0	0	81	844	0	925
2019-10-18b	-32.2 (-8.9)	-17.8	-39.1	1092	146	81	844	0	2163
2019-10-21	-2.9 (-0.8)	3.6	-17.6	2.5	2.0	0	71	81	467	1	620
2019-10-23	1.6 (0.4)	6.0	-15.3	3.0	2.6	0	71	81	0	1	153
2019-10-28	0.0 (0.0)	7.5	-13.8	2.8	2.4	0	71	81	842	1	995
2020-02-13	-0.2 (-0.1)	11.1	-10.2	3.8	3.3	405	142	81	840	1	1469

81 points as shown in Column (9). The data from the SwRI robotic telescopes are noted in Column (10). The full time range of the data spans from 2019 June 29 to October 13. The first three orbit fits have a shorter data set owing to an earlier cutoff date for this data source. The number of occultation points used is given in Column (11). For Orus we only had data from the OR20190907 event. Note that for the first three orbits with an occultation point we used a positional uncertainty of 1 km, while the last one used an uncertainty of 2 km. These uncertainties are certainly too small, but we needed to overweight the data to keep the orbit estimates consistent with the OR20190907 result. Column (12) gives the total number of astrometric points used in the fit.

The information in Table 20 summarizes some important trends that affected our prediction work. At the very start is the one and only orbit fit we did to predict the OR20190907 occultation. That prediction worked extremely well as confirmed by the observations in Oman. At that point, our confidence level was very high that we had a process that would give us a prediction we could trust for the OR20191104 event. After all, the S01 chord was at 3.6 km from the predicted centerline with an uncertainty of 2.7 km. That result seemed to be quite reasonable. However, the very next prediction on 2019 October 2 showed a large shift and was inconsistent with the successful occultation. The two changes made for that prediction were adding all of the MPC data and an additional month of data from SRO. Thinking that the MPC data might be causing a problem, we dropped those data the next week while adding another week of data from SRO. Unfortunately, the shift was still present. Starting on 2019 October 16, we tried a number of experiments to localize what was causing the shift. No firm conclusions were possible other than that there were significant systematic errors present.

The biggest breakthrough came with the addition of the occultation-based astrometric constraint from OR20190907, even though that was a single-chord result. The length of the chord strongly suggests that S01 was near the centerline, likely closer than the uncertainty of the star position. We did not have any rigorous way to establish an uncertainty on the position, so instead we adjusted the uncertainty so that the final orbit fit was consistent with the OR20190907 observation. With an uncertainty too large, the vastly larger number of other astrometric measurements dominated the fit and gave a result inconsistent with the occultation, just as with all the prior orbit fits starting with 2019 October 2. We adjusted the uncertainty downward until we basically replicated the 2019 August 29

prediction and thus were consistent with the occultation. With the 2019 October 21 prediction, we felt that we once again had a useful orbit estimate to work with. From there we could then examine the different data sets for a sign of systematic errors, assuming that the occultation data were correct. No systematic errors were uncovered in the Gaia data. The PS2 data also showed no systematic errors, though the uncertainties here are higher than for Gaia, making this search somewhat harder. The MPC data continued to be troublesome to include and were left out of the final prediction for the OR20191104 event. The SRO data, however, showed a clear signature of a systematic error at the 10 mas level. This error can be seen in Figure 26. The residuals in this figure are shown against the 2019 October 23 orbit fit. Each point represents the robust average of the residuals for each night of data, and if there are less than three good points, a given night is discarded. The data in both cases come from the same nights, but the bad-point filtering from the robust average can lead to different results on each night. The variation in uncertainties is driven largely by the number of measurements that are averaged. This particular fit is especially diagnostic since it contains the occultation astrometry and does not contain the SRO data. As seen on the top row of the figure, there is clearly an offset in the residuals, 7.5 mas in R.A. and 13.1 mas in decl. These numbers map to errors on the plane of the sky of about 30–40 km and are important for the occultation predictions. After implementing the differential refraction correction, the offset in the residuals drops to zero.

Note that it is easy for the residuals at a given site to be systematically off owing to ignoring the differential refraction correction. If the astrometry from one site is a large-enough data set on its own, it can be hard to see the problem. Having data from multiple sites at different latitudes can help reveal these systematic effects and also make it clear when the differential refraction correction is applied properly. We have seen that our simplified method using the mean color of the reference stars used along with the filter employed for the observation is good enough, for now. Note that our software can use a color from almost any pair of filters since we only try to estimate the mean wavelength.

This high-precision work carries with it some important requirements. It is essential that all data have accurate absolute uncertainties. Our approach here uses the scatter of many measurements within a night to provide an empirical measurement of the uncertainties. This method cannot provide true uncertainties on a single measurement but works very well when characterizing the uncertainty on the average of a set.

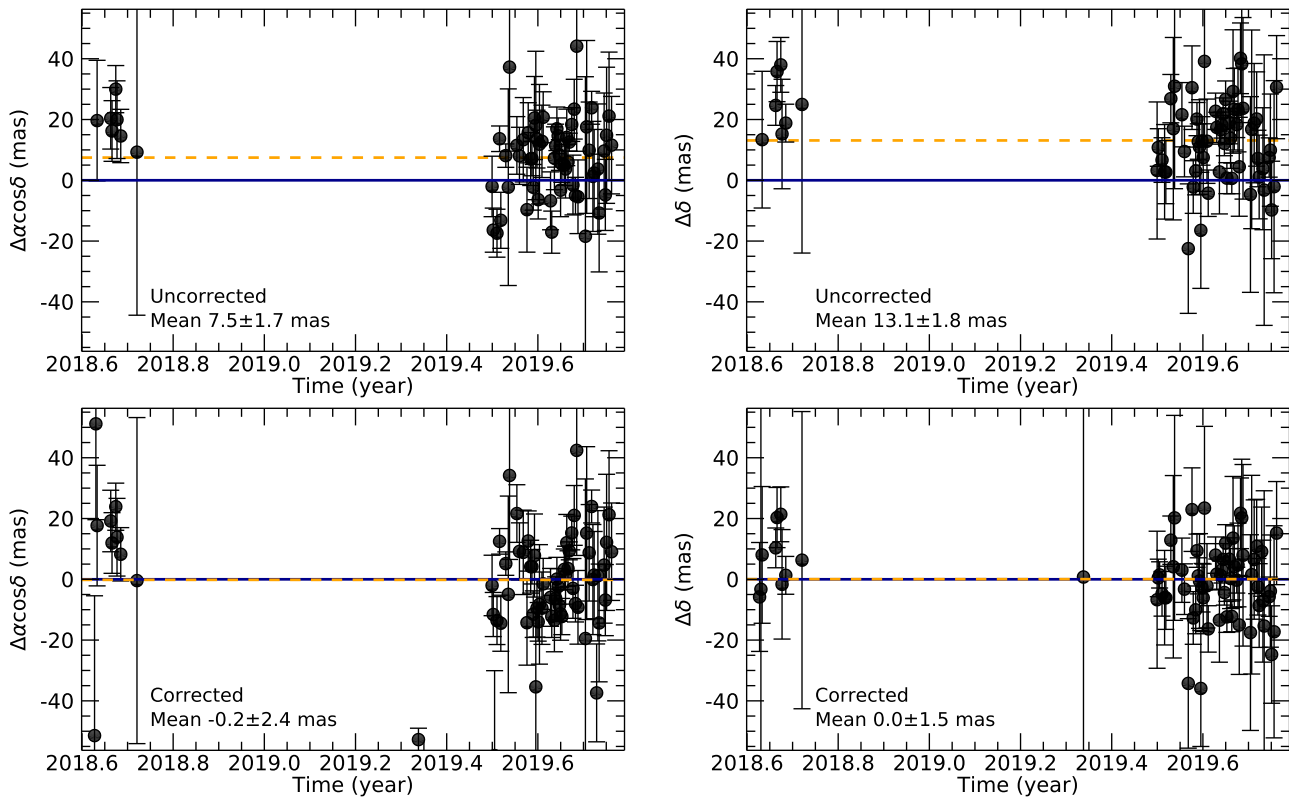


Figure 26. Residuals of Orus astrometry from SRO. The top row shows the residuals of the uncorrected SRO astrometry relative to the 2019 October 23 orbit fit. The bottom row shows the same data after the correction for differential refraction is applied. The mean of the residual (dashed orange line) and the standard deviation of the mean are indicated in each panel. The zero reference level is highlighted with a dark-blue line. All data points are shown, though some error bars are clipped to optimize the scale for showing the points. Differences in plotted points are a consequence of different bad-point filtering between the two cases.

After averaging, the uncertainties can become small enough that the number of significant digits used in the long-standing MPC OBS80 data format is insufficient. Taking full advantage of our data requires using the new ADES format for both reporting and retrieving observations. Doing so ensures that the precision of the data is maintained, as well as providing the uncertainties. To make full use of reported data, it is no longer sufficient to just report the position at some time even if the full precision is maintained. Supporting data become important for knowing whether the data are already corrected for refraction or not. If not, then the mean reference star color and filter used are also important. Common practice is to report a standardized magnitude (e.g., V or R), but this correction requires knowing the actual passband of the filter, and the latter information is not always provided. In cases where there are a lot of data handled in a similar fashion (e.g., Pan-STARRS), the differential refraction correction can be worked out knowing the rough field of view of the instrument and the photometric depth of the reference stars used.

ORCID iDs

- Marc W. Buie [ID](https://orcid.org/0000-0003-0854-745X) <https://orcid.org/0000-0003-0854-745X>
- Brian A. Keeney [ID](https://orcid.org/0000-0003-0797-5313) <https://orcid.org/0000-0003-0797-5313>
- Simon B. Porter [ID](https://orcid.org/0000-0003-0333-6055) <https://orcid.org/0000-0003-0333-6055>
- Lawrence H. Wasserman [ID](https://orcid.org/0000-0001-5769-0979) <https://orcid.org/0000-0001-5769-0979>
- Robert J. Weryk [ID](https://orcid.org/0000-0002-0439-9341) <https://orcid.org/0000-0002-0439-9341>
- Harold F. Levison [ID](https://orcid.org/0000-0001-5847-8099) <https://orcid.org/0000-0001-5847-8099>
- Catherine B. Olkin [ID](https://orcid.org/0000-0002-5846-716X) <https://orcid.org/0000-0002-5846-716X>
- Rodrigo Leiva [ID](https://orcid.org/0000-0002-6477-1360) <https://orcid.org/0000-0002-6477-1360>

- Michael E Brown [ID](https://orcid.org/0000-0002-8255-0545) <https://orcid.org/0000-0002-8255-0545>
- David W. Dunham [ID](https://orcid.org/0000-0001-7527-4207) <https://orcid.org/0000-0001-7527-4207>
- Megan, T. Gilluca [ID](https://orcid.org/0000-0002-2587-0841) <https://orcid.org/0000-0002-2587-0841>
- P. C. Hinton [ID](https://orcid.org/0000-0001-9504-0520) <https://orcid.org/0000-0001-9504-0520>
- Timothy R. Holt [ID](https://orcid.org/0000-0003-0437-3296) <https://orcid.org/0000-0003-0437-3296>
- Joshua A. Kammer [ID](https://orcid.org/0000-0002-3441-3757) <https://orcid.org/0000-0002-3441-3757>
- Theodore Karetta [ID](https://orcid.org/0000-0003-1008-7499) <https://orcid.org/0000-0003-1008-7499>
- John M. Keller [ID](https://orcid.org/0000-0002-0915-4861) <https://orcid.org/0000-0002-0915-4861>
- John N. Kidd, Jr. [ID](https://orcid.org/0000-0002-4010-3050) <https://orcid.org/0000-0002-4010-3050>
- Tod R. Lauer [ID](https://orcid.org/0000-0003-3234-7247) <https://orcid.org/0000-0003-3234-7247>
- Franck Marchis [ID](https://orcid.org/0000-0001-7016-7277) <https://orcid.org/0000-0001-7016-7277>
- Kelly E. Miller [ID](https://orcid.org/0000-0001-5657-137X) <https://orcid.org/0000-0001-5657-137X>
- Beatrice E. A. Mueller [ID](https://orcid.org/0000-0001-6194-3174) <https://orcid.org/0000-0001-6194-3174>
- J. W. Noonan [ID](https://orcid.org/0000-0003-2152-6987) <https://orcid.org/0000-0003-2152-6987>
- Michael J. Person [ID](https://orcid.org/0000-0003-0000-0572) <https://orcid.org/0000-0003-0000-0572>
- Julien J. Salmon [ID](https://orcid.org/0000-0002-5977-3724) <https://orcid.org/0000-0002-5977-3724>
- R. P. Sawyer [ID](https://orcid.org/0000-0002-1064-9132) <https://orcid.org/0000-0002-1064-9132>
- Alessondra Springmann [ID](https://orcid.org/0000-0001-6401-0126) <https://orcid.org/0000-0001-6401-0126>
- Anne J. Verbiscer [ID](https://orcid.org/0000-0002-3323-9304) <https://orcid.org/0000-0002-3323-9304>
- Qicheng Zhang [ID](https://orcid.org/0000-0002-6702-191X) <https://orcid.org/0000-0002-6702-191X>

References

- Belskaya, I. N., Barucci, M. A., Fulchignoni, M., & Dovgopol, A. N. 2015, *Icar*, 250, 482
- Bernstein, G. M., Trilling, D. E., Allen, R. L., et al. 2004, *AJ*, 128, 1364
- Brown, A. G. A., Vallenari, A., Prusti, T., et al. 2018, *A&A*, 616, A1
- Buie, M. W., & Keller, J. M. 2016, *AJ*, 151, 73
- Buie, M. W., Porter, S. B., Tamblyn, P., et al. 2020, *AJ*, 159, 130
- Buie, M. W., Spencer, J. R., Parker, A. H., et al. 2012, *LPICo*, 1667, 6430

- Buie, M. W., Zangari, A. M., Marchi, S., Levison, H. F., & Mottola, S. 2018, *AJ*, **155**, 245
- Chambers, K. C., Magnier, E. A., Metcalfe, N., et al. 2016, arXiv:1612.05560
- Cochran, A. L., Levison, H. F., Stern, S. A., & Duncan, M. J. 1995, *ApJ*, **455**, 342
- CRC Handbook 2007, CRC Handbook of Chemistry and Physics (88th ed.; Boca Raton, FL: CRC Press)
- Dangl, G. 2013, JOA, 03, 3
- DeMeo, F. E., Alexander, C. M. O., Walsh, K. J., Chapman, C. R., & Binzel, R. P. 2015, in Asteroids IV, ed. P. Michel, F. E. DeMeo, & W. F. Bottke (Tucson, AZ: Univ. Arizona Press), 13
- DeMeo, F. E., Binzel, R. P., Slivan, S. M., & Bus, S. J. 2009, *Icar*, **202**, 160
- Durech, J., Kaasalainen, M., Herald, D., et al. 2011, *Icar*, **214**, 652
- Eisele, J. A., & Shannon, P. E. V. 1975, Atmospheric Refraction Corrections for Optical Sightings of Astronomical Objects, Naval Research Lab. Memorandum Report 3058
- Emery, J. P., Marzari, F., Morbidelli, A., French, L. M., & Grav, T. 2015, in Asteroids IV, ed. P. Michel, F. E. DeMeo, & W. F. Bottke (Tucson, AZ: Univ. Arizona Press), 203
- Filippenko, A. V. 1982, *PASP*, **94**, 715
- Fornasier, S., Dotto, E., Hainaut, O., et al. 2007, *Icar*, **190**, 622
- Grav, T., Mainzer, A. K., Bauer, J. M., Masiero, J. R., & Nugent, C. R. 2012, *ApJ*, **759**, 49
- Green, R. M. 1985, Spherical Astronomy (Cambridge: Cambridge Univ. Press)
- Hanuš, J., Viikinkoski, M., Marchis, F., et al. 2017, *A&A*, **601**, A114
- Holt, T. R., Nesvorný, D., Horner, J., et al. 2020, *MNRAS*, **495**, 4085
- Lauer, T. R., Throop, H. B., Showalter, M. R., et al. 2018, *Icar*, **301**, 155
- Leiva, R., Buie, M. W., Keller, J. M., et al. 2020, *PSJ*, **1**, 48
- Levison, H. F., Olkin, C. B., Noll, K., Marchi, S. & Lucy Team 2017, LPSC, **48**, 2025
- Marchi, S., Chapman, C. R., Barnouin, O. S., Richardson, J. E., & Vincent, J. B. 2015, in Asteroids IV, ed. P. Michel, F. E. DeMeo, & W. F. Bottke (Tucson, AZ: Univ. Arizona Press), 725
- Marchi, S., McSween, H. Y., O'Brien, D. P., et al. 2012, *Sci*, **336**, 690
- Marchis, F., Malvache, A., Marfisi, L., Borot, A., & Arbouch, E. 2020, AcAau, **166**, 23
- Mottola, S., Hellmich, S., Buie, M. W., et al. 2020, *PSJ*, **1**, 73
- Nautical Almanac Offices of the United Kingdom and the United States of America 1974, Explanatory Supplement to the Astronomical Ephemeris and the American Ephemeris and Nautical Almanac (London: Her Majesty's Stationery Office)
- Nesvorný, D. 2018, *ARA&A*, **56**, 137
- Noll, K., Grundy, W., Buie, M., Levison, H. F., & Marchi, S. 2018, AAS/DPS Meeting, **50**, 217.04
- Porter, S. B., Buie, M. W., Parker, A. H., et al. 2018, *AJ*, **156**, 20
- Satō, I., Buie, M., Maley, P. D., et al. 2014, *IJAA*, **4**, 91
- Stone, R. C. 2002, *PASP*, **114**, 1070
- Tedesco, E. F., Noah, P. V., Noah, M., & Price, S. D. 2002, *AJ*, **123**, 1056
- Veres, P., Farnocchia, D., Chesley, S. R., & Chamberlin, A. B. 2017, *Icar*, **296**, 139
- Wong, I., & Brown, M. E. 2016, *AJ*, **152**, 90